Geochimica et Cosmochimica Acta 367 (2024) 142–164

Contents lists available at ScienceDirect

Geochimica et Cosmochimica Acta

journal homepage: www.elsevier.com/locate/gca

Partitioning of nickel and cobalt between metal and silicate melts: Expanding the oxy-barometer to reducing conditions

Camille Cartier [a], Laurie Llado [a,b], Hadrien Pirotte [b], Laurent Tissandier [a], Olivier Namur [c], Max Collinet [d], Shui-Jiong Wang [e], Bernard Charlier [b]

[a] Université de Lorraine, CNRS, CRPG, F-54000 Nancy, France
[b] Department of Geology, University of Liège, 4000 Sart Tilman, Belgium
[c] Department of Earth and Environmental Sciences, KU Leuven, 3001 Heverlee, Belgium
[d] Département de géologie, UNamur, Rue de Bruxelles, 61, 5000 Namur, Belgium
[e] State Key Laboratory of Geological Processes and Mineral Resources, China University of Geosciences (Beijing), Beijing 100083, China

ARTICLE INFO

Associate editor: Rajdeep Dasgupta

Keywords:
Magma ocean
Planetary differentiation
Moderately siderophile elements
Core formation
Achondrites

ABSTRACT

Moderately siderophile elements (MSEs) are potential tracers of the thermodynamic conditions prevailing during planetary core formation because their metal–silicate partition coefficients ($D^{met/sil}$) vary as a function of P, T, and oxygen fugacity (fO_2). Those properties result in the production of planetary mantles with unique MSE depletion signatures. Among the MSEs, Ni and Co are reliable barometers in magma oceans because their $D^{met/sil}$ values are strongly correlated with pressure, decreasing by almost 3 orders of magnitude between 1 bar and 100 GPa. Current pressure-dependent expressions of $D^{met/sil}$ were calibrated based on experiments performed under relatively oxidizing conditions, mostly at fO_2 slightly below the iron–wüstite Fe–FeO buffer (IW), which is relevant to the mantles of Earth and Mars. However, planets and asteroids formed under a wide range of redox conditions, from Mercury, the most reduced (~IW − 5.5), to the most oxidized angrite parent body (IW − 1.5 to IW + 1). In this study, we performed and analyzed 38 metal–silicate partitioning experiments over a wide range of pressures (1 bar to 26 GPa) and oxygen fugacities (IW − 6.4 to IW − 1.9) to expand the available Ni and Co $D^{met/sil}$ values to reducing conditions. We then parameterized 255 Ni and 194 Co $D^{met/sil}$ values as a function of T (1573–5700 K), P (1 bar to 100 GPa), and fO_2 (IW − 6.4 to IW + 0.2). We also modeled the evolution of Ni and Co $D^{met/sil}$ values along the liquidus of a chondritic mantle at various P and fO_2 conditions to investigate the thermodynamic conditions of various planetary bodies' magma oceans. The P and fO_2 conditions we obtained for Earth, Mars, the Moon, and Vesta are consistent with previous studies using similar methods, and the pressure during core formation is strongly correlated to planetary size. Finally, we also applied our model to several achondrite parent bodies; our results indicate a wide variety of objects, from the asteroid-sized, oxidized angrite parent body to the planet-sized, highly reduced aubrite parent body.

1. Introduction

The distribution of elements between the cores and mantles of planets and differentiated asteroids was primarily established by high pressure and high temperature metal–silicate partitioning during core segregation in a magma ocean context (Rubie et al., 2003; Righter, 2015). Moderately siderophile elements (MSEs) serve as valuable indicators of the thermodynamic conditions prevailing during core formation because their metal–silicate partition coefficients ($D^{met/sil}$) vary based on pressure (P), temperature (T), and oxygen fugacity (fO_2). As a result, planetary mantles exhibit distinct MSE depletion patterns that provide insights into their formation processes. Accordingly, much effort has been dedicated to understanding the composition of the bulk silicate Earth and Mars, and to constraining their differentiation by investigating metal–silicate reactions between liquid metal and liquid silicates at high P and T (Righter and Drake, 1996; Wade and Wood, 2005; Rubie et al., 2011; Fischer et al., 2015). Among the MSEs, Ni and Co are reliable barometers for application to magma oceans because their $D^{met/sil}$ values are strongly correlated to pressure, decreasing by almost 3 orders of magnitude between 1 bar and 100 GPa (Righter, 2011; Fischer et al., 2015). Using parameterized Ni and Co $D^{met/sil}$ values, previous studies found metal–silicate equilibrium pressures of

E-mail address: camille.cartier@univ-lorraine.fr (C. Cartier).

https://doi.org/10.1016/j.gca.2023.12.020
Received 24 July 2023; Accepted 15 December 2023
Available online 23 December 2023

30–60 GPa for Earth (Li and Agee, 2001; Wade and Wood, 2005; Bouhifd and Jephcoat, 2011; Siebert et al., 2012; Fischer et al., 2015) and 7–17 GPa for Mars (Righter et al., 1998; Righter and Chabot, 2011; Brennan et al., 2020). These pressures, recording metal–silicate equilibrium at mantellic liquidus temperatures, are 5–78 % lower than those estimated at the present-day core–mantle boundaries (CMBs) from geophysical measurements (136 GPa for Earth; Dehant et al., 2022; 18–21 GPa for Mars; Rivoldini et al., 2011; Stähler et al., 2021).This large difference indicates that planetary embryos were not fully molten during the last stages of their accretion (Rubie et al., 2003, 2011; Righter, 2015; Brennan et al., 2020).

Current pressure-dependent expressions of $D^{met/sil}$ were calibrated on experiments performed under relatively oxidizing conditions (Wade and Wood, 2005; Bouhifd and Jephcoat, 2011; Fischer et al., 2015; Righter, 2015), mostly slightly below the iron–wüstite Fe–FeO buffer (IW), corresponding to the redox conditions of the terrestrial and Martian mantles (Righter et al., 2020). However, recent experiments at very low fO_2 suggest that Ni and Co $D^{met/sil}$ values are also strongly dependent on fO_2 (Steenstra et al., 2020a, b), although their experiments were conducted at only a single pressure (1 GPa). The behavior of Ni and Co at reducing high-pressure conditions therefore remains unknown. Because planets and asteroids formed at a wide range of redox conditions from Mercury, the most reduced (~IW − 5.5; Namur et al., 2016; Cartier and Wood, 2019), to the most oxidized angrite parent body (IW − 1.5 to IW + 1; Righter et al., 2016; Tissot et al., 2022), a new parameterization of $D^{met/sil}$ for Co and Ni under reducing conditions and spanning a broad range of pressures is critically needed.

In this study, we performed 38 metal–silicate partitioning experiments over a wide range of pressures (1 bar to 26 GPa) and oxygen fugacities (IW − 6.4 to IW − 1.9) to expand the available Ni and Co $D^{met/sil}$ values to reducing conditions. Of the 38 experiments, 21 are published here for the first time; the other 17 were reported in Cartier et al., (2014a, 2014b), Bouhifd et al. (2015), and Pirotte et al. (2023). To construct a tool applicable to most planetary conditions, we compiled our new data with the experimental partitioning database of Fischer et al. (2015) and Huang and Badro (2018), to which we added recent studies conducted under highly reducing conditions (see Section 3.2). We then parameterized Ni and Co $D^{met/sil}$ as a function of T, P, and fO_2. Our new model reliably predicts the evolution of Ni and Co $D^{met/sil}$ values from 1 bar to 80 GPa, IW to IW − 6, and 1550–4450 K. Finally, we

Table 1
Experimental parameters and results. Abbreviations: sil. melt, silicate melt; met., metal; sulf., sulfide; Bdm, bridgmanite; Maj, majorite; Sti, stishovite; En, enstatite; Fo, forsterite; Coe, coesite; Qtz, quartz. fO_2 is reported relative to IW, calculated assuming ideal behavior of Fe and FeO, and is estimated to have errors of ± 1 log unit (see Section 2.7). (*) indicates experiments previously published in Cartier et al., (2014a, 2014b), Bouhifd et al. (2015), and Pirotte et al. (2023).

Run	Device	P (GPa)	T (K)	Duration	ΔIW	Result	X_S Metal	NBO/T
#143	MA	26	2400	45 min	−2.4	Sil. melt, met., Bdm	0.2733	2.53
#176A (*)	MA	26	2444	40 min	−2.4	Sil. melt, met.	0.1741	1.82
#177 (*)	MA	26	2410	35 min	−3.3	Sil. melt, met., Maj, Bdm., Sti	0.2245	2.02
#178	MA	26	2075	30 min	−2.8	Sil. melt, met.	0.4858	2.41
#195	MA	26	2345	20 min	−5.4	Sil. melt, met., Maj, Bdm., Sti	0.0892	1.82
#197	MA	26	2357	30 min	−2.1	Sil. melt, met., Maj, Bdm, Sti	0.3925	1.95
#198	MA	26	2360	30 min	−3.0	Sil. melt, met.	0.4739	1.80
#205	MA	26	2349	35 min	−5.6	Sil. melt, met., Maj, Bdm, Sti	0.1219	1.89
1083c (*)	MA	5	1883	3.5 h	−5.4	Sil. melt, met., sulf., En	0.0049	1.08
1093b (*)	MA	5	1953	4 h	−4.9	Sil. melt, met., sulf., En	0.0132	0.89
1133 (*)	MA	5	1963	3.5 h	−4.9	Sil. melt, met., sulf., En	0.0157	1.31
1135 (*)	MA	5	1923	2.5 h	−4.9	Sil. melt, met., sulf., En	0.0048	1.05
1136b (*)	MA	5	1913	2 h	−4.4	Sil. melt, met., sulf., En, Coe	0.0252	0.80
1137 (*)	MA	5	1973	3 h	−1.9	Sil. melt, met., sulf., En	0.1008	1.65
1162 (*)	MA	5	1923	2.5 h	−5.3	Sil. melt, met., En	0.0001	1.29
1178 (*)	MA	5	1853	2 h	−6.4	Sil. melt, met., En, Coe	0.0003	1.20
1183 (*)	MA	5	1993	2.25 h	−2.1	Sil. melt, met., sulf., En	0.0549	1.72
1188	MA	5	1963	2 h	−4.8	Sil. melt, met., sulf., En	0.0180	1.74
1198 (*)	MA	5	2073	3 h	−1.9	Sil. melt, met., sulf., En	0.0385	1.23
1210 (*)	MA	5	2073	3 h	−4.7	Sil. melt, met., sulf., En	0.0138	1.36
1212 (*)	MA	5	2123	3 h	−4.7	Sil. melt, met., sulf., En	0.0214	0.99
A022	PC	1.3	1873	1 h	−5.1	Sil. melt, met.	0.0007	1.36
A023	PC	1.3	1773	2 h	−5.1	Sil. melt, met.	0.0020	1.34
A038	PC	1.3	1873	45 min	−4.7	Sil. melt, sulf., Qtz	0.5029	0.76
A040	PC	1.3	1973	45 min	−4.7	Sil. melt, sulf	0.5030	0.79
A041	PC	2	1973	45 min	−4.3	Sil. melt, sulf., Qtz	0.5064	0.97
A043	PC	1.3	1873	45 min	−3.5	Sil. melt, sulf.	0.5066	0.94
B873	PC	3	1973	3 h	−2.1	Sil. melt, met.	0.0005	1.60
B879 (*)	PC	3	1973	3 h	−4.6	Sil. melt, met.	0.0047	1.64
YO37-2 (*)	IHPV	0.1	1873	3 h	−4.1	Sil. melt, sulf.	0.0026	1.31
YO56-1	IHPV	0.1	1793	3 h	−5.1	Sil. melt, met., sulf.	0.0164	1.38
YO83-2 (*)	IHPV	0.1	1793	3 h	−5.0	Sil. melt, met., sulf.	0.0082	1.44
YO43-2	IHPV	0.1	1793	3 h	−4.8	Sil. melt, met., sulf.	0.0002	1.31
FM165	EST	0.0001	1673	5 h	−5.5	Sil. melt, met., sulf., En, Fo	0.0013	1.36
FM161	EST	0.0001	1573	48 h	−5.6	Sil. melt, met., sulf., En, Fo	0.0185	0.66
FM167	EST	0.0001	1623	24 h	−5.5	Sil. melt, met., sulf., En, Fo	0.0234	1.19
FM153	EST	0.0001	1623	48 h	−5.4	Sil. melt, met., sulf., En, Fo	0.0047	0.93
FM152	EST	0.0001	1623	24 h	−5.3	Sil. melt, met., sulf., En, Fo	0.0075	1.09

apply our model to investigate the prevailing thermodynamic conditions of various planetary bodies' magma oceans, including Earth, Mars, the Moon, and various achondrite parent bodies.

2. Materials and methods

Metal–silicate partitioning experiments were performed on various starting chondritic compositions using multi-anvil and piston-cylinder apparatuses, internally heated pressure vessels (IHPVs), and evacuated silica tubes (ESTs) in various institutes (Table 1). Some of the 5 GPa and 26 GPa experiments were published in previous studies but the remaining experiments are published here for the first time (Cartier et al., 2014a; Bouhifd et al., 2015; Pirotte et al., 2023). Details on each method and experimental series are provided in the following subsections.

2.1. Multi-anvil experiments

Experiments were performed at 5 or 26 GPa with multi-anvil presses at the Laboratoire Magmas et Volcans (LMV, Clermont-Ferrand, France) using a natural enstatite chondrite starting powder (Hvittis, EL6; composition given by Rubin, 1983; Table S1), except for experiment 1198, which used a natural tholeiitic basalt powder. Various amounts of Si metal (0–50 wt%) were added to the experiments to reduce the instrinsic fO_2 (Table S2). Experiments at 26 GPa were performed using a 1,500 t multi-anvil press, and those at 5 GPa using a 1,000 t press. Pressure calibrations were similar to those described previously for the 1,000 t press by Hammouda (2003) and for the 1,500 t press by Boujibar et al. (2014). The pressure assemblies consisted of Cr-doped MgO octahedra of 18, 14, or 10 mm edge lengths for 5 GPa experiments or 10 mm edge lengths for 26 GPa experiments, compressed between pyrophyllite gaskets by 32 mm tungsten carbide anvils with truncation edge lengths of 11, 8, or 4 mm, respectively. Samples were contained in graphite capsules that transformed to diamond in the 26 GPa experiments, except for experiment 1188 that was run in a MgO capsule. The assembled octahedra were dried in an oven at 500 K overnight before each experiment. The samples were first compressed to the desired pressure at room temperature with an uncertainty of ~ 0.5 GPa, then heated to the target temperature and held isothermally for durations of 20 min to 4 h (Table 1). At the pressure–temperature conditions of the experiments, these durations are sufficient to achieve equilibrium between silicate and metallic liquids (Li and Agee, 2001; Bouhifd and Jephcoat, 2011). A $LaCrO_3$ heater insulated by ZrO_2 sleeves was used to heat the samples, and the temperature was monitored using type-C ($W_5Re_{95}/W_{26}Re_{74}$) thermocouples with no correction for the pressure effect on the electromotive force, yielding an uncertainty of ± 100 K. In cases when the thermocouple broke, temperature was determined using the power–temperature relation determined in previous experiments. Samples were quenched at a rate of approximately 800 K/s by shutting off the power.

2.2. Piston-cylinder experiments

Experiments at 1.3, 2, and 3 GPa were performed on a piston-cylinder apparatus. The starting material was a synthetic powder representative of the silicate portion of enstatite chondrites (Lodders and Fegley, 1998; Berthet et al., 2009) prepared from high purity oxides (TiO_2, Al_2O_3, Cr_2O_3, MnO, MgO, $CaSiO_3$, Na_2SiO_3, $K_2Si_{14}O_9$, $AlPO_4$), to which different amounts and combinations of Fe, Si, FeS, and/or CaS were added (Tables S3, S4), resulting in low intrinsic fO_2 conditions (Table 1). The starting powder was doped with 500 ppm Ni and 500 ppm Co. The 1.3 and 2 GPa experiments were conducted at the University of Liège (Belgium) using barium carbonate cells and graphite capsules. The cells were pressurized to 0.75 GPa at room temperature, heated to 865 °C, held for 5 min, pressurized to the target pressure, and finally heated to the target temperature (1500–1700 °C). We used type-D ($W_3Re_{97}/W_{75}Re_{25}$) thermocouples to monitor temperature. The difference between the measured temperature and the sample temperature was estimated to be around 20 °C. Samples were held at the target temperature for 45 min to 3 h depending on the temperature (Table 1), then quenched by shutting off the electrical current. The 3 GPa experiments were performed at the Bayerisches Geoinstitut (University of Bayreuth, Germany) using talc-Pyrex pressure cells and graphite capsules inside outer platinum capsules; the experimental protocol was similar that for the 1.3 and 2 GPa experiments at 1700 °C.

2.3. Internally heated pressure vessel experiments

Experiments at 0.1 GPa were performed using IHPVs at the University of Hannover (Germany) with the same starting powders used in the piston-cylinder experiments (Section 2.2; Table S5). The apparatus and experimental protocol are detailed in Berndt et al. (2002) and Namur et al. (2016), respectively, and summarized here. We used graphite capsules surrounded by platinum jackets. Thin (0.1 mm) Pt wire was used to place the sample in the hotspot of the furnace. Pressure was increased to 0.1 GPa using argon as the pressure medium before heating. Two type-S ($Pt/Pt_{90}Rh_{10}$) thermocouples were used to control the temperature at the top and bottom of the cell, and two others were used to monitor the sample temperature. The experiments were run for 3 h at1520–1600 °C (Table 1). Samples were quenched by applying a current to the Pt wire, causing the sample to fall onto a room-temperature, water-cooled copper plate at the bottom of the furnace.

2.4. Evacuated silica tubes experiments

EST experiments were performed at the Centre de Recherches Pétrographiques et Géochimiques (CRPG, Nancy, France). The starting compositions consisted of two natural chondrite powders: carbonaceous chondrite NWA 11345 (CM2) and ordinary chondrite Tamdakht (H5). The bulk chemical major and trace element compositions of these powders were measured at the Service d'Analyse des Roches et des Minéraux (CRPG, Nancy) using a procedure involving alkali fusion, inductively coupled plasma mass spectrometry (ICP-MS), and liquid chromatography ICP-MS (Carignan et al., 2001) (Table S6). The experimental charges comprised graphite crucibles containing the chondritic powder that were placed within 1.5 to 3 cm^3 sealed silica tubes. Before the experiments, the silica tubes were sealed on one side, evacuated under vacuum at 10^{-2} mbar and 120 °C during 24 h, then sealed on the other side. Once sealed, the silica tubes were introduced into a muffle furnace at the target temperature (1300–1400 °C). Experiment durations were between 5 and 48 h depending on the temperature. During the experiments, the oxygen in the sample reacted with the carbon in the crucible to produce carbon monoxide gas, theoretically buffering the fO_2 at C–CO (i.e. IW − 5.8 at 1300 °C to IW − 6.4 at 1400 °C; fO_2 calculated with NIST-JANAF thermodynamic tables, see Supplementary Materials for details). The experiments were quenched by removing the tube from the furnace.

2.5. SEM imaging and microprobe major and minor element analyses

Once quenched, all experiments were mounted in epoxy and polished for chemical analyses. Backscattered electron (BSE) images and energy-dispersive X-ray spectroscopy (EDS) chemical maps were acquired with a JEOL 6510 scanning electron microscope (SEM) at the CRPG. Major and minor element contents in the metal and silicate phases of the 26 GPa, 5 GPa, and EST experiments were analyzed with a CAMECA SX100 electron microprobe at the LMV using an accelerating voltage of 15 kV (Table 2). Silicate glasses were analyzed using a 4nA beam current, whereas metal and sulfides were analyzed with a 15nA beam. The beam was defocused to 5–20 μm. The oxygen concentrations of most glasses were measured with microprobe using a PC1 crystal with on-peak counting times of 15 s. Otherwise, when not measured, oxygen

Table 2
Chemical compositions of silicate melts and metal and sulfide phases in experiments and corresponding metal–silicate and sulfide–silicate partition coefficients. Major and minor elements were measured by microprobe, and Ni and Co by LA-ICP-MS. Na, number of analyzes; n.a., not analyzed; b.d.l., below detection limit; *, analytical error.

Run	**#143**		**#176A**		**#177**		**#178**		**#195**		**#197**		**#198**		**#205**	
ΔIW	−2.4		−2.4		−3.3		−2.8		−5.4		−2.1		−3.0		−5.6	
P(GPa)/T (K)	26	2400	26	2444	26	2050	26	2075	26	2345	26	2357	26	2360	26	2349
Part. Coef.	*D*	*1σ*	*D*	*1σ*	*D*	*1σ*	*D*	*1σ*	*D*	*1σ*	*D*	*1σ*	*D*	*1σ*	*D*	*1σ*
D_{Ni} met/sil	265	57.0	148	29.4	412	30.3	163	37.5	4485	1441	156	94.1	399	250.6	3756	442
D_{Ni} sulf/sil	–	–	–	–	–	–	–	–	–	–	–	–	–	–	–	–
D_{Co} met/sil	105	41.8	–	–	–	–	–	–	–	–	203	41.7	–	–	–	–
D_{Co} sulf/sil	–	–	–	–	–	–	–	–	–	–	–	–	–	–	–	–
silicate melt																
EPMA wt%	*Na = 3*	*1σ*	*Na = 5*	*1σ*	*Na = 3*	*1σ*	*Na = 5*	*1σ*	*Na = 4*	*1σ*	*Na = 4*	*1σ*	*Na = 4*	*1σ*	*Na = 4*	*1σ*
Si	20.79	0.30	26.45	0.77	25.45	0.23	22.05	0.41	27.13	0.49	25.64	0.10	26.87	0.17	24.85	0.69
Ti	0.00	0.00	0.08	0.02	0.01	0.02	0.00	0.00	0.03	0.01	0.06	0.02	0.03	0.02	0.05	0.04
Al	0.83	0.03	1.09	0.04	0.62	0.03	0.67	0.02	0.96	0.10	0.77	0.04	1.13	0.06	1.03	0.09
Cr	3.36	0.10	0.21	0.03	0.59	0.03	2.95	0.08	0.00	0.00	0.36	0.05	0.21	0.02	0.00	0.00
Fe	2.01	0.04	4.61	0.51	1.52	0.11	1.20	0.04	0.11	0.02	5.30	0.67	1.50	0.09	0.08	0.03
Mn	0.08	0.01	0.14	0.04	0.08	0.04	0.07	0.02	0.00	0.00	0.27	0.04	0.09	0.01	0.01	0.03
Mg	22.32	0.16	19.11	0.67	20.99	0.17	22.63	0.51	19.77	0.33	17.63	0.28	20.65	0.28	18.83	0.26
Ca	1.07	0.08	1.28	0.22	1.72	0.02	1.01	0.05	3.23	0.38	3.17	0.04	1.13	0.10	3.04	0.20
Na	0.42	0.04	0.52	0.07	0.55	0.02	0.40	0.04	1.44	0.38	1.31	0.28	0.54	0.08	1.69	0.25
K	0.06	0.01	0.05	0.04	0.12	0.02	0.05	0.01	0.24	0.12	0.19	0.04	0.04	0.00	0.29	0.21
Ni	0.02	0.02	0.06	0.01	0.04	0.02	0.01	0.03	0.01	0.01	0.01	0.02	0.02	0.03	0.02	0.02
S	0.23	0.02	0.03	0.03	0.04	0.02	0.15	0.04	1.19	0.65	0.03	0.02	0.21	0.03	2.92	0.53
La	4.28	0.01	0.03	0.03	1.81	0.13	2.56	0.14	0.12	0.02	0.29	0.20	0.33	0.18	0.24	0.25
O	40.2	0.43	44.71	1.40	43.57	0.97	43.11	2.34	47.88	1.02	45.14	0.20	46.79	0.70	45.81	1.48
Total	95.67	0.40	98.36	1.61	97.11	0.51	96.86		102.11	2.49	100.17	0.73	99.56	0.33	98.86	1.76
LA-ICPMS ppm	*Na = 5*	*1σ*	*Na = 5*	*1σ*	*Na = 6*	*1σ*	*Na = 4*	*1σ*	*Na = 6*	*1σ*	*Na = 4*	*1σ*	*Na = 5*	*1σ*	*Na = 1*	*1σ**
Ni	203.9	6.2	482.0	38.0	129.0	4.0	115.3	3.5	8.7	2.6	317.4	79.1	107.4	3.4	9.7	0.9
Co	20.3	0.5	n.a.	–	n.a.	–	n.a.	–	b.d.l.	–	33.7	5.9	11.5	0.6	b.d.l.	–
Metal																
EPMA wt%	*Na = 2*	*1σ*	*Na = 5*	*1σ*	*Na = 2*	*1σ*	*Na = 4*	*1σ*	*Na = 5*	*1σ*	*Na = 5*	*1σ*	*Na = 6*	*1σ*	*Na = 4*	*1σ*
Si	0.03	0.03	0.03	0.02	0.01	0.00	0.07	0.08	20.25	5.88	0.05	0.02	0.07	0.03	23.07	0.56
Ti	0.03	0.01	0.01	0.01	0.01	0.01	0.05	0.06	0.04	0.05	0.01	0.02	0.00	0.01	n.a.	–
Al	n.a.	–	n.a.	–	n.a.	–	n.a.	–	0.01	0.01	0.01	0.01	0.00	0.00	n.a.	–
Cr	27.04	8.82	0.10	0.04	2.67	0.29	25.16	1.98	0.32	0.21	0.05	0.01	1.63	0.68	1.04	0.27
Fe	39.67	1.32	76.79	1.94	71.26	0.98	34.36	2.67	65.01	1.34	65.63	4.10	56.58	1.20	61.22	0.70
Mn	0.26	0.24	0.01	0.01	0.12	0.05	0.14	0.01	0.28	0.13	0.02	0.02	0.11	0.05	n.a.	–
Mg	0.00	0.00	0.00	0.00	0.01	0.00	0.08	0.07	0.03	0.05	0.01	0.02	0.05	0.02	n.a.	–
Ca	0.01	0.01	0.02	0.02	0.02	0.02	0.02	0.01	0.02	0.02	0.02	0.01	0.02	0.01	n.a.	–
Ni	5.40	1.15	7.13	1.30	5.31	0.35	1.88	0.43	3.91	0.43	4.94	2.72	4.29	2.69	3.64	0.27
S	19.63	5.14	10.45	2.08	14.51	0.77	36.02	1.11	6.65	5.25	27.17	7.77	34.31	2.66	8.91	0.80
O	4.78	3.75	0.73	0.08	2.23	0.18	0.77	0.22	2.41	0.73	0.75	0.17	1.01	0.21	n.a.	–
Total	96.84	0.51	95.28	0.93	96.17	0.11	98.54	1.14	98.94	1.27	98.72	1.31	98.07	2.76	98.01	0.28
LA-ICPMS ppm	*Na = 2*	*1σ*	*Na = 5*	*1σ*	*Na = 6*	*1σ*			*Na = 3*	*1σ*	*Na = 2*	*1σ*			*Na = 3*	*1σ*
Ni	50,606	12,728	92,535	58,661	43,522	14,787	n.a.	–	36,452	5100	105,098	3635	n.a.	–	37,314	8825
Co	2134.8	847.6	n.a.	–	n.a.	–	n.a.	–	2128	344	6844	736	n.a.	–	1736	302
Sulfide																
EPMA wt%																
Si	–	–	–	–	–	–	–	–	–	–	–	–	–	–	–	–
Ti	–	–	–	–	–	–	–	–	–	–	–	–	–	–	–	–
Al	–	–	–	–	–	–	–	–	–	–	–	–	–	–	–	–
Cr	–	–	–	–	–	–	–	–	–	–	–	–	–	–	–	–

(*continued on next page*)

Table 2 (*continued*)

Run	**#143**		**#176A**		**#177**		**#178**		**#195**		**#197**		**#198**		**#205**	
ΔIW	−2.4		−2.4		−3.3		−2.8		−5.4		−2.1		−3.0		−5.6	
P(GPa)/T (K)	26	2400	26	2444	26	2050	26	2075	26	2345	26	2357	26	2360	26	2349
Fe	–	–	–	–	–	–	–	–	–	–	–	–	–	–	–	–
Mn	–	–	–	–	–	–	–	–	–	–	–	–	–	–	–	–
Mg	–	–	–	–	–	–	–	–	–	–	–	–	–	–	–	–
Ca	–	–	–	–	–	–	–	–	–	–	–	–	–	–	–	–
Ni	–	–	–	–	–	–	–	–	–	–	–	–	–	–	–	–
S	–	–	–	–	–	–	–	–	–	–	–	–	–	–	–	–
O	–	–	–	–	–	–	–	–	–	–	–	–	–	–	–	–
Total	–	–	–	–	–	–	–	–	–	–	–	–	–	–	–	–
LA-ICPMS ppm																
Ni	–	–	–	–	–	–	–	–	–	–	–	–	–	–	–	–
Co	–	–	–	–	–	–	–	–	–	–	–	–	–	–	–	–

Run	**1083c**		**1093b**		**1133**		**1135**		**1136b**		**1137**		**1162**		**1178**	
ΔIW	−5.4		−4.9		−4.9		−4.9		−4.4		−1.9		−5.3		−6.4	
P(GPa)/T(K)	5	1883	5	1953	5	1963	5	1923	5	1913	5	1973	5	1923	5	1853
Part. Coef.	*D*	*1σ*	*D*	*1σ*	*D*	*1σ*	*D*	*1σ*	*D*	*1σ*	*D*	*1σ*	*D*	*1σ*	*D*	*1σ*
D_{Ni} met/sil	8396	1746	12,230	5286	6385	1448	9168	1793	6690	1999	938	241.1	3955	1191	31,042	8218
D_{Ni} sulf/sil	84	33.8	740	357	361	212	860	747	1426	942	200	115.1	–		–	
D_{Co} met/sil	–	–	–	–	–	–	–	–	–	–	–	–	–	–	–	–
D_{Co} sulf/sil	–	–	–	–	–	–	–	–	–	–	–	–	–	–	–	–
silicate melt																
EPMA wt%	*Na=4*	*1σ*	*Na=5*	*1σ*	*Na=3*	*1σ*	*Na=3*	*1σ*	*Na=3*	*1σ*	*Na=2*	*1σ*	*Na=7*	*1σ*	*Na=4*	*1σ*
Si	27.56	0.17	28.33	0.22	29.93	0.18	30.66	0.63	31.60	0.33	23.78	0.15	31.30	1.10	28.63	0.20
Ti	0.10	0.03	0.07	0.04	0.06	0.04	0.05	0.04	0.05	0.03	0.25	0.02	0.01	0.02	0.02	0.01
Al	2.71	0.06	3.47	0.17	1.51	0.04	2.09	0.05	2.91	0.15	2.44	0.01	1.14	0.07	2.00	0.03
Cr	0.07	0.03	0.09	0.03	0.01	0.01	0.03	0.03	0.02	0.02	0.28	0.04	0.02	0.02	0.04	0.03
Fe	0.12	0.03	0.23	0.08	0.28	0.03	0.24	0.05	0.50	0.05	8.61	0.34	0.09	0.05	0.03	0.02
Mn	0.13	0.04	0.19	0.06	0.09	0.02	0.14	0.04	0.05	0.04	0.28	0.01	0.04	0.04	0.01	0.01
Mg	11.85	0.13	9.25	1.00	17.27	0.16	13.76	0.06	10.28	0.31	13.60	0.13	17.70	0.80	15.15	0.25
Ca	4.07	0.07	5.50	0.44	1.37	0.09	2.21	0.07	2.86	0.07	2.85	0.09	1.15	0.12	1.80	0.07
Na	1.73	0.11	1.74	0.10	0.55	0.07	1.05	0.09	1.69	0.02	1.37	0.11	0.43	0.05	0.93	0.06
K	0.46	0.03	0.72	0.03	0.10	0.07	0.20	0.03	0.39	0.04	0.35	0.06	0.08	0.02	0.14	0.04
Ni	0.02	0.03	0.08	0.02	0.02	0.02	0.00	0.00	0.01	0.01	0.02	0.02	0.01	0.03	0.00	0.01
S	8.97	0.26	5.18	0.52	1.96	0.10	3.79	0.09	0.37	0.05	0.03	0.03	2.82	0.36	10.10	0.13
La	n.a.	–	n.a.	–	n.a.	–	n.a.	–	n.a.	–	n.a.	–	n.a.	–	n.a.	–
O	39.54	0.28	43.12	0.10	46.44	0.12	41.04	0.39	46.18	0.32	43.86	0.13	51.79	0.88	39.51	0.53
Total	97.34	0.86	97.96	0.16	99.58	0.33	95.26	0.49	96.90	0.73	97.71	0.28	106.58	1.50	98.37	0.66
LA-ICPMS ppm	*Na=4*	*1σ*	*Na=2*	*1σ*	*Na=3*	*1σ*	*Na=3*	*1σ*	*Na=5*	*1σ*	*Na=3*	*1σ*	*Na=2*	*1σ*	*Na=4*	*1σ*
Ni	5.9	1.1	4.4	1.9	8	1.8	5.67	0.85	8.4	2.5	70.4	8.3	8.9	2.5	1.02	0.27
Co	n.a.	–	n.a.	–	n.a.	–	n.a.	–	n.a.	–	n.a.	–	n.a.	–	n.a.	–
Metal																
EPMA wt%	*Na=4*	*1σ*	*Na=3*	*1σ*	*Na=3*	*1σ*	*Na=4*	*1σ*	*Na=3*	*1σ*	*Na=3*	*1σ*	*Na=4*	*1σ*	*Na=4*	*1σ*
Si	22.21	1.13	16.60	0.18	12.43	1.71	16.96	0.47	4.34	0.11	0.01	0.00	42.57	1.19	41.21	0.21
Ti	0.01	0.00	0.01	0.01	0.01	0.01	0.00	0.00	0.01	0.00	0.00	0.01	0.05	0.02	0.05	0.02
Al	n.a.	–	n.a.	–	0.00	0.00	n.a.	–	n.a.	–	0.01	0.00	n.a.	–	0.00	0.00
Cr	0.30	0.09	0.19	0.02	0.19	0.03	0.16	0.08	0.17	0.02	0.06	0.01	0.37	0.04	0.22	0.02
Fe	71.52	0.75	75.22	0.45	78.75	0.70	75.89	1.11	82.15	0.30	81.95	0.47	53.36	0.44	54.45	0.45
Mn	0.01	0.00	0.01	0.01	0.00	0.00	0.01	0.01	0.01	0.01	0.00	0.01	0.31	0.02	0.19	0.03
Mg	0.00	0.00	0.00	0.01	0.01	0.01	0.01	0.01	0.00	0.00	0.01	0.00	0.01	0.01	0.01	0.00
Ca	0.00	0.00	0.01	0.01	0.01	0.01	n.a.	–	0.00	0.00	0.01	0.00	0.01	0.01	0.00	0.00
Ni	4.95	0.46	5.38	0.10	5.11	0.14	5.20	0.65	5.62	0.15	6.60	1.51	3.52	0.38	3.17	0.01
S	0.35	0.05	0.88	0.08	1.01	0.07	0.32	0.08	1.46	0.13	5.75	2.37	0.01	0.01	0.03	0.02
O	0.25	0.01	0.21	0.01	0.44	0.32	0.07	0.07	0.51	0.02	0.24	0.02	0.31	0.08	0.03	0.02
Total	99.61	0.29	98.51	0.26	97.96	0.77	98.62	0.50	94.28	0.17	94.65	0.36	100.54	0.97	99.58	0.55
LA-ICPMS ppm	*Na=4*	*1σ*	*Na=3*	*1σ*	*Na=3*	*1σ*	*Na=2*	*1σ*	*Na=5*	*1σ*	*Na=3*	*1σ*	*Na=6*	*1σ*	*Na=4*	*1σ*
Ni	39,443	2059	58,900	9390	43,606	6219	44,956	4522	61,301	2685	49,543	12,110	44,163	13,301	29,296	1068
Co	n.a.	–	n.a.	–	n.a.	–	n.a.	–	n.a.	–	n.a.	–	n.a.	–	n.a.	–
Sulfide																
EPMA wt%	*Na=3*	*1σ*	*Na=3*	*1σ*	*Na=3*	*1σ*	*Na=3*	*1σ*	*Na=5*	*1σ*	*Na=3*	*1σ*	–	–	–	–
Si	0.02	0.01	0.12	0.13	0.50	0.27	1.28	1.46	0.54	0.43	0.02	0.00	–	–	–	–
Ti	1.53	0.08	0.72	0.12	0.54	0.15	0.62	0.29	0.44	0.21	0.01	0.01	–	–	–	–
Al	n.a.	–	n.a.	–	n.a.	–	n.a.	–	n.a.	–	n.a.	–	–	–	–	–

(*continued on next page*)

Table 2 (*continued*)

Run	**1083c**		**1093b**		**1133**		**1135**		**1136b**		**1137**		**1162**		**1178**	
ΔIW	−5.4		−4.9		−4.9		−4.9		−4.4		−1.9		−5.3		−6.4	
P(GPa)/T(K)	5	1883	5	1953	5	1963	5	1923	5	1913	5	1973	5	1923	5	1853
Cr	3.33	0.14	2.70	0.41	2.96	0.59	4.02	1.18	1.77	0.61	0.18	0.07	–	–	–	–
Fe	14.30	0.85	56.31	0.80	57.26	0.27	54.24	2.52	62.24	3.49	62.16	0.46	–	–	–	–
Mn	5.90	0.30	1.65	0.16	1.73	0.17	1.54	0.24	1.17	0.36	0.03	0.02	–	–	–	–
Mg	22.41	0.61	0.05	0.07	0.01	0.01	0.35	0.52	0.01	0.01	0.00	0.00	–	–	–	–
Ca	2.29	0.08	0.00	0.00	0.01	0.02	0.02	0.01	0.00	0.00	0.01	0.01	–	–	–	–
Ni	0.05	0.02	0.33	0.07	0.29	0.16	0.49	0.42	1.20	0.71	1.41	0.79	–	–	–	–
S	46.73	0.53	36.33	0.56	36.38	0.81	34.50	3.36	30.00	5.48	35.31	1.89	–	–	–	–
O	1.12	0.53	0.16	0.06	n.a.	–	n.a.	–	0.47	0.03	n.a.	–	–	–	–	–
Total	97.69	1.17	98.38	1.26	99.69	1.16	97.07	2.43	97.85	1.55	99.15	0.82	–	–	–	–
LA-ICPMS ppm			*Na=1*	*1σ**	*Na=2*	*1σ*	*Na=2*	*1σ*	*Na=2*	*1σ*	*Na=3*	*1σ*				
Ni	n.a.	–	14,447	2222	43,092	9641	15,458	4754	56,453	12,556	40,569	3567	–	–	–	–
Co	n.a.	–	n.a.	–	n.a.	–	n.a.	–	n.a.	–	n.a.	–	–	–	–	–

Run	**1183**		**1188**		**1198**		**1210**		**1212**		**A022**		**A023**		**A038**	
ΔIW	−2.1		−4.8		−1.9		−4.7		−4.7		−5.1		−5.1		−4.7	
P(GPa)/T(K)	5	1993	5	1963	5	2073	5	2073	5	2123	1.3	1873	1.3	1773	1.3	1873
Part. Coef.	*D*	*1σ*	*D*	*1σ*	*D*	*1σ*	*D*	*1σ*	*D*	*1σ*	*D*	*1σ*	*D*	*1σ*	*D*	*1σ*
D_{Ni} met/sil	811	142.2	2360	277.5	584	143.2	5350	617.4	8511	806.2	3455	764.4	3060	404.2	–	–
D_{Ni} sulf/sil	913	158.1	106	37.9	552	239.7	675	171.1	2094	1290.5	–	–	–	–	–	–
D_{Co} met/sil	75	13.9	–	–	–	–	–	–	662	473.9	5525	1889.0	5426	1764.5	–	–
D_{Co} sulf/sil	61	9	–	–	–	–	–	–	53	33	–	–	–	–	898	339
silicate melt																
EPMA wt%	*Na=6*	*1σ*	*Na=4*	*1σ*	*Na=4*	*1σ*	*Na=4*	*1σ*	*Na=4*	*1σ*	*Na=11*	*1σ*	*Na=11*	*1σ*	*Na=8*	*1σ*
Si	24.38	0.36	23.08	0.62	19.22	0.15	29.48	0.15	30.93	0.33	26.96	0.28	26.43	0.14	33.06	0.51
Ti	0.15	0.03	0.06	0.01	0.40	0.04	0.03	0.03	0.07	0.03	0.01	0.01	0.01	0.01	0.01	0.01
Al	2.14	0.17	3.05	0.31	8.10	0.08	1.43	0.08	2.25	0.06	1.16	0.02	1.67	0.11	2.30	0.57
Cr	0.26	0.06	0.00	0.01	0.05	0.05	0.02	0.02	0.02	0.02	0.11	0.03	0.12	0.02	0.01	0.01
Fe	7.89	0.62	0.26	0.08	10.02	0.23	0.37	0.08	0.36	0.08	0.22	0.07	0.21	0.03	0.20	0.05
Mn	0.19	0.04	0.13	0.02	0.10	0.02	0.13	0.04	0.15	0.06	0.23	0.02	0.24	0.03	0.05	0.02
Mg	15.36	0.34	15.69	1.99	8.78	0.16	17.38	0.18	12.81	0.18	11.60	0.25	11.30	0.16	11.53	0.91
Ca	1.98	0.08	5.08	0.38	7.53	0.15	1.28	0.06	2.44	0.08	8.21	0.27	8.49	0.16	0.82	0.05
Na	1.26	0.05	3.79	0.42	1.44	0.03	0.81	0.05	1.24	0.08	0.65	0.03	0.78	0.03	0.93	0.13
K	0.27	0.10	0.58	0.07	0.04	0.03	0.10	0.04	0.23	0.02	0.14	0.02	0.12	0.02	0.14	0.02
Ni	0.03	0.03	0.02	0.01	0.01	0.01	0.01	0.01	0.01	0.02	0.00	0.00	0.00	0.00	0.03	0.04
S	0.11	0.06	n.a.	–	0.13	0.05	2.04	0.13	1.35	0.10	8.28	0.30	8.41	0.16	2.46	0.14
La	n.a.	–	n.a.	–	n.a.	–	n.a.	–	n.a.	–	n.a.	–	n.a.	–	n.a.	–
O	45.10	0.97	37.39	0.27	43.06	0.09	45.82	0.05	46.53	0.86	42.45	0.85	42.22	0.84	48.45	0.97
Total	99.12	1.00	89.15	0.77	98.86	0.65	98.90	0.24	98.07	0.55	100.66	0.37	100.70	0.21	99.63	0.33
LA-ICPMS ppm	*Na=5*	*1σ*	*Na=2*	*1σ*	*Na=5*	*1σ*	*Na=4*	*1σ*	*Na=4*	*1σ*	*Na=8*	*1σ*	*Na=10*	*1σ*	*Na=11*	*1σ*
Ni	64.7	2.3	22.4	2.6	1.28	0.29	7.95	0.81	6.04	0.5	0.9	0.2	1.0	0.2	b.d.l.	–
Co	44.1	5.6	n.a.	–	n.a.	–	n.a.	–	2.8	1.4	0.4	0.1	0.4	0.1	0.3	0.1
Metal																
EPMA wt%	*Na=3*	*1σ*	*Na=4*	*1σ*	*Na=4*	*1σ*	*Na=4*	*1σ*	*Na=4*	*1σ*	*Na=8*	*1σ*	*Na=7*	*1σ*	–	–
Si	0.00	0.01	14.48	0.32	0.00	0.00	10.11	0.13	8.43	0.27	13.81	0.32	12.83	0.44	–	–
Ti	0.01	0.01	0.01	0.01	0.02	0.02	0.01	0.02	0.01	0.01	0.01	0.01	0.03	0.07	–	–
Al	0.00	0.01	0.00	0.00	0.00	0.00	0.00	0.00	0.00	0.00	n.a.	–	n.a.	–	–	–
Cr	0.11	0.01	0.19	0.05	0.01	0.02	0.26	0.09	0.34	0.07	2.33	0.08	2.25	0.18	–	–
Fe	83.26	1.45	76.90	0.54	92.07	0.54	81.18	0.58	80.26	0.61	77.84	0.35	78.41	2.64	–	–
Mn	0.01	0.00	0.05	0.05	0.01	0.02	0.02	0.03	0.03	0.02	0.02	0.01	0.03	0.03	–	–
Mg	0.00	0.00	0.01	0.01	0.00	0.00	0.01	0.01	0.00	0.00	0.00	0.00	0.00	0.00	–	–
Ca	0.01	0.01	0.00	0.00	0.02	0.01	0.00	0.00	0.01	0.01	0.02	0.02	0.04	0.04	–	–
Ni	5.25	0.90	5.29	0.10	0.07	0.01	4.25	0.23	5.14	0.24	0.30	0.02	0.31	0.04	–	–
S	2.97	0.95	1.18	0.28	2.12	0.23	0.85	0.34	1.29	0.19	0.04	0.02	0.13	0.33	–	–
O	0.20	0.04	0.27	0.03	0.00	0.00	0.00	0.00	0.00	0.00	n.a.	–	n.a.	–	–	–
Total	91.82	0.68	98.37	0.49	94.34	0.67	96.70	0.69	95.51	0.21	96.49	0.32	95.95	2.15	–	–

(*continued on next page*)

Table 2 (*continued*)

Run	**1183**		**1188**		**1198**		**1210**		**1212**		**A022**		**A023**		**A038**	
ΔIW	−2.1		−4.8		−1.9		−4.7		−4.7		−5.1		−5.1		−4.7	
P(GPa)/ T(K)	5	1993	5	1963	5	2073	5	2073	5	2123	1.3	1873	1.3	1773	1.3	1873
LA-ICPMS ppm	*Na=4*	*1σ*	*Na=4*	*1σ*	*Na=4*	*1σ*	*Na=3*	*1σ*	*Na=4*	*1σ*	*Na=3*	*1σ*	*Na=7*	*1σ*		
Ni	66,314	4044	52,069	1801	765	69	13,369	2937	61,559	3436	2788	135	2630	130	–	–
Co	3304	449	n.a.	–	n.a.	–	n.a.	–	1885	955	1990	136	2048	52	–	–
Sulfide																
EPMA wt%	*Na=2*	*1σ*	*Na=1*	*1σ**	*Na=2*	*1σ*	*Na=1*	*1σ**	*Na=4*	*1σ*	–	–	–	–	*Na=7*	*1σ*
Si	0.01	0.00	0.08	0.03	0.00	0.00	0.44	0.05	0.04	0.07	–	–	–	–	0.01	0.01
Ti	0.01	0.01	0.06	0.06	0.01	0.01	0.27	0.08	0.31	0.11	–	–	–	–	0.30	0.13
Al	0.00	0.00	0.01	0.02	0.00	0.00	0.02	0.03	0.00	0.00	–	–	–	–	0.00	0.00
Cr	0.09	0.05	1.36	0.14	0.03	0.03	3.22	0.20	2.38	0.43	–	–	–	–	2.31	0.49
Fe	69.53	1.67	60.47	0.87	68.18	1.83	57.18	0.84	58.59	1.45	–	–	–	–	57.96	0.77
Mn	0.01	0.01	0.54	0.08	0.00	0.00	0.92	0.13	0.79	0.10	–	–	–	–	0.81	0.13
Mg	0.00	0.00	0.00	0.03	0.02	0.01	0.41	0.07	0.03	0.01	–	–	–	–	0.15	0.04
Ca	0.00	0.00	0.00	0.05	0.01	0.01	0.07	0.04	0.02	0.01	–	–	–	–	0.01	0.01
Ni	5.91	1.00	0.24	0.08	0.07	0.03	0.54	0.12	1.26	0.77	–	–	–	–	0.03	0.01
S	21.48	3.19	36.44	0.69	31.55	1.57	35.90	1.01	35.88	1.79	–	–	–	–	36.61	0.27
O	0.40	0.01	0.28	0.13	0.29	0.03	1.05	0.12	0.00	0.00	–	–	–	–	n.a.	–
Total	97.43	0.59	99.47	–	100.15	0.22	100.01	–	99.30	0.19	–	–	–	–	98.20	0.32
LA-ICPMS ppm	*Na=2*	*1σ*	–	–	*Na=3*	*1σ*	*Na=2*	*1σ*	*Na=4*	*1σ*					*Na=14*	*1σ*
Ni	55,263	16,068	n.a.	–	965	178	48,434	5647	4256	1801	–	–	–	–	419	108
Co	2709	206	n.a.	–	n.a.	–	n.a.	–	151	56	–	–	–	–	260	50

Run	**A040**		**A041**		**A043**		**B873**		**B879**		**Y037-2**		**Y056-1**		**Y083-2**	
ΔIW	−4.7		−4.3		−3.5		−2.1		−4.6		−4.1		−5.1		−5.0	
P(GPa)/T(K)	1.3	1973	2	1973	1.3	1873	3.0	1973	3.0	1973	0.1	1873	0.1	1793	0.1	1793
Part. Coef.	*D*	*1σ*	*D*	*1σ*	*D*	*1σ*	*D*	*1σ*	*D*	*1σ*	*D*	*1σ*	*D*	*1σ*	*D*	*1σ*
D_{Ni} met/sil	–	–	–	–	–	–	570	191.5	1928	510.7	3471	3266.0	4614	1523.3	3454	1163.1
D_{Ni} sulf/sil	–	–	28	34.8	152	73.9	–	–	172	183.2	368	237.0	399	230.9	517	307.9
D_{Co} met/sil	–	–	–	–	–	–	192	18.2	2059	145.8	473	103.3	4948	1114.9	5374	1502.0
D_{Co} sulf/sil	800	118	397	447	329	91	–	–	388	100	240	55	1009	235	905	257
silicate melt																
EPMA wt%	*Na=8*	*1σ*	*Na=8*	*1σ*	*Na=8*	*1σ*	*Na=5*	*1σ*	*Na=6*	*1σ*	*Na=6*	*1σ*	*Na=6*	*1σ*	*Na=7*	*1σ*
Si	34.16	0.34	32.12	0.29	32.34	0.19	26.16	0.14	25.49	0.18	29.45	0.37	28.80	0.11	28.22	0.14
Ti	0.01	0.01	0.01	0.01	0.05	0.01	0.08	0.01	0.01	0.01	0.06	0.01	0.04	0.01	0.03	0.01
Al	1.09	0.02	1.26	0.02	1.10	0.02	1.24	0.05	1.98	0.08	1.36	0.03	1.41	0.02	1.43	0.02
Cr	0.01	0.01	0.03	0.02	0.05	0.01	0.44	0.02	0.04	0.02	0.05	0.01	0.02	0.01	0.05	0.02
Fe	0.22	0.09	0.36	0.12	0.88	0.07	8.21	0.10	0.45	0.19	0.84	0.08	0.27	0.10	0.31	0.08
Mn	0.08	0.02	0.10	0.02	0.12	0.02	0.30	0.02	0.19	0.03	0.10	0.01	0.08	0.02	0.11	0.02
Mg	11.46	0.34	13.09	0.28	12.64	0.13	14.72	0.31	18.58	0.40	16.46	0.24	17.23	0.07	17.59	0.14
Ca	0.80	0.12	0.90	0.04	0.84	0.03	1.02	0.04	1.18	0.17	1.09	0.03	1.16	0.02	1.16	0.03
Na	0.88	0.15	1.22	0.23	0.90	0.02	0.91	0.08	1.45	0.10	1.10	0.03	1.15	0.04	1.16	0.03
K	0.15	0.02	0.16	0.02	0.14	0.01	0.16	0.02	0.19	0.02	0.18	0.01	0.19	0.01	0.18	0.02
Ni	0.04	0.06	0.00	0.00	0.02	0.03	0.00	0.00	0.00	0.00	0.00	0.00	0.01	0.01	0.01	0.01
S	2.76	0.07	3.22	0.07	0.82	0.05	0.00	0.00	12.50	0.30	1.55	0.04	2.68	0.05	4.88	0.10
La	n.a.	–	n.a.	–	n.a.	–	n.a.	–	n.a.	–	n.a.	–	n.a.	–	n.a.	–
O	48.34	0.97	47.52	0.95	50.08	1.00	46.76	0.94	37.94	0.76	47.76	0.96	46.96	0.94	44.88	0.90
Total	99.86	0.77	99.78	0.53	97.36	0.39	97.45	0.39	106.32	0.47	99.05	1.28	99.51	0.27	101.19	0.30
LA-ICPMS ppm	*Na=11*	*1σ*	*Na=12*	*1σ*	*Na=12*	*1σ*	*Na=9*	*1σ*	*Na=7*	*1σ*	*Na=7*	*1σ*	*Na=8*	*1σ*	*Na=8*	*1σ*
Ni	b.d.l.	–	5.4	3.1	2.2	0.7	1.7	0.3	0.68	0.11	1.0	0.4	0.4	0.0	0.5	0.0
Co	0.4	0.1	0.8	0.8	1.7	0.4	15.6	1.2	0.36	0.02	1.4	0.3	0.3	0.1	0.3	0.1
Metal																
EPMA wt%	–	–	–	–	–	–	*Na=11*	*1σ*	*Na=11*	*1σ*	*Na=3*	*1σ*	*Na=11*	*1σ*	*Na=13*	*1σ*
Si	–	–	–	–	–	–	0.01	0.01	14.95	0.95	b.d.l.	–	0.85	0.47	5.27	1.72
Ti	–	–	–	–	–	–	0.00	0.00	0.00	0.01	0.00	0.00	0.01	0.01	0.01	0.01
Al	–	–	–	–	–	–					0.01	0.02				
Cr	–	–	–	–	–	–	0.17	0.05	0.03	0.01	0.56	0.03	0.09	0.10	0.24	0.09
Fe	–	–	–	–	–	–	89.09	0.47	82.90	0.84	98.04	0.43	90.60	3.19	89.05	2.07
Mn	–	–	–	–	–	–	0.00	0.01	0.00	0.00	b.d.l.	–	0.02	0.05	0.02	0.02
Mg	–	–	–	–	–	–	0.00	0.00	0.00	0.01	b.d.l.	–	0.01	0.01	0.00	0.00
Ca	–	–	–	–	–	–	0.01	0.01	0.00	0.01	0.00	0.02	0.00	0.01	0.01	0.01
Ni	–	–	–	–	–	–	0.10	0.03	0.13	0.03	0.34	0.29	0.21	0.07	0.16	0.05

(*continued on next page*)

Table 2 (*continued*)

Run	A040		A041		A043		B873		B879		Y037-2		Y056-1		Y083-2	
ΔIW	−4.7		−4.3		−3.5		−2.1		−4.6		−4.1		−5.1		−5.0	
P(GPa)/T(K)	1.3	1973	2	1973	1.3	1873	3.0	1973	3.0	1973	0.1	1873	0.1	1793	0.1	1793
S	–	–	–	–	–	–	0.03	0.01	0.31	0.08	0.15	0.04	0.92	1.78	0.49	0.30
O	–	–	–	–	–	–					n.a.	–				
Total	–	–	–	–	–	–	91.83	0.42	99.25	0.30	98.99	0.45	94.69	1.79	97.14	0.57
LA-ICPMS ppm							*Na=4*	*1σ*	*Na=5*	*1σ*	*Na=3*	*1σ*	*Na=3*	*1σ*	*Na=4*	*1σ*
Ni	–	–	–	–	–	–	1213	211	1457	166	723	153	1639	206	1391	56
Co	–	–	–	–	–	–	2988	163	737	22	662	25	1731	97	1412	61
Sulfide																
EPMA wt%	*Na=8*	*1σ*	*Na=7*	*1σ*	*Na=10*	*1σ*	–	–	*Na=8*	*1σ*	*Na=5*	*1σ*	*Na=6*	*1σ*	*Na=5*	*1σ*
Si	0.01	0.00	0.02	0.01	0.01	0.01	–	–	0.04	0.04	0.00	0.00	0.01	0.01	0.01	0.01
Ti	0.24	0.07	0.39	0.13	0.03	0.02	–	–	0.35	0.20	0.09	0.02	0.18	0.12	0.64	0.30
Al	0.00	0.00	0.00	0.00	0.00	0.00	–	–	0.00	0.00	0.00	0.00	0.00	0.00	0.00	0.00
Cr	1.73	0.30	2.56	0.29	1.63	0.25	–	–	2.68	0.69	2.06	0.25	1.69	0.67	3.86	0.75
Fe	58.87	0.58	57.32	0.61	59.26	0.42	–	–	57.70	1.16	58.96	0.45	59.13	0.83	56.57	1.29
Mn	0.76	0.05	0.91	0.10	0.62	0.05	–	–	0.47	0.10	0.87	0.02	0.75	0.10	0.93	0.04
Mg	0.16	0.03	0.14	0.03	0.01	0.01	–	–	0.18	0.05	0.28	0.04	0.13	0.03	0.22	0.02
Ca	0.02	0.02	0.00	0.00	0.00	0.00	–	–	0.01	0.01	0.01	0.01	0.02	0.02	0.01	0.01
Ni	0.03	0.01	0.02	0.02	0.03	0.02	–	–	0.01	0.01	0.04	0.02	0.02	0.01	0.02	0.01
S	36.16	0.58	36.50	0.39	36.41	0.13	–	–	37.29	0.34	37.26	0.06	37.08	0.27	37.34	0.09
O	n.a.	–	n.a.	–	n.a.	–	–	–	n.a.	–	n.a.	–	n.a.	–	n.a.	–
Total	97.99	0.49	97.88	0.59	98.04	0.33	–	–	98.74	0.44	99.57	0.29	99.01	0.37	99.61	0.23
LA-ICPMS ppm	*Na=12*	*1σ*	*Na=7*	*1σ*	*Na=13*	*1σ*			*Na=10*	*1σ*	*Na=9*	*1σ*	*Na=9*	*1σ*	*Na=7*	*1σ*
Ni	545	57	464	52	759	121	–	–	295	144	447	36	568	35	401	34
Co	353	26	298	45	543	64	–	–	139	35	336	26	353	28	238	16

Run	YO43-2		FM165		FM161		FM167		FM153		FM152	
ΔIW	−4.8		−5.5		−5.6		−5.5		−5.4		−5.3	
P(GPa)/T(K)	0.1	1793	0.0001	1673	0.0001	1573	0.0001	1623	0.0001	1623	0.0001	1623
Part. Coef.	*D*	*1σ*	*D*	*1σ*	*D*	*1σ*	*D*	*1σ*	*D*	*1σ*	*D*	*1σ*
D_{Ni} met/sil	–	–	41,016	34,049	36,670	13,052	21,375	11,521	19,220	11,816	19,739	9123
D_{Ni} sulf/sil	–	–	890	790	6129	3273	3964	2213	1510	877	569	246
D_{Co} met/sil	3967	1292.6	2056	706.8	–	–	–	–	–	–	–	–
D_{Co} sulf/sil	640	289	–	–	–	–	–	–	–	–	–	–
silicate melt												
EPMA wt%	*Na=8*	*1σ*	*Na=4*	*1σ*	*Na=3*	*1σ*	*Na=3*	*1σ*	*Na=3*	*1σ*	*Na=5*	*1σ*
Si	29.68	0.29	25.57	0.42	27.96	0.12	25.68	0.17	18.84	0.12	18.90	0.01
Ti	0.04	0.01	0.16	0.01	0.12	0.04	0.12	0.01	0.05	0.01	0.05	0.01
Al	1.45	0.04	4.26	0.95	7.16	0.11	5.55	0.01	4.37	0.86	3.83	0.46
Cr	0.03	0.05	0.03	0.02	0.01	0.01	0.05	0.02	0.01	0.01	0.02	0.02
Fe	0.42	0.15	0.14	0.03	0.13	0.00	0.14	0.01	0.12	0.03	0.13	0.02
Mn	0.09	0.05	0.18	0.13	0.17	0.03	0.31	0.10	0.05	0.03	0.05	0.04
Mg	16.77	0.23	15.76	2.24	9.52	0.29	15.42	0.07	9.02	1.88	10.23	1.18
Ca	1.15	0.05	6.23	1.28	5.99	0.14	4.94	0.13	3.89	0.46	3.66	0.47
Na	1.09	0.06	b.d.l.	–	0.01	0.00	0.01	0.01	0.00	0.00	0.00	0.00
K	0.16	0.01	0.01	0.00	0.00	0.00	0.01	0.01	0.00	0.00	0.00	0.00
Ni	n.a.	–	0.01	0.01	0.03	0.01	0.03	0.00	b.d.l	–	b.d.l	–
S	2.48	0.12	3.30	0.51	0.77	0.06	2.14	0.06	2.11	0.37	1.85	0.14
La	n.a.	–	n.a.	–	n.a.	–	n.a.	–	n.a.	–	n.a.	–
O	49.11	0.98	49.29	0.20	47.90	0.38	48.79	0.19	61.59	0.35	61.36	0.18
Total	100.57	1.07	104.92	0.58	100.01	0.76	103.46	0.36	100.00	0.00	100.00	0.00
LA-ICPMS ppm	*Na=2*	*1σ*	*Na=5*	*1σ*	*Na=2*	*1σ*	*Na=3*	*1σ*	*Na=3*	*1σ*	*Na=5*	*1σ*
Ni	b.d.l.	–	1.82	1.51	1.41	0.19	3.51	1.89	3.73	1.62	3.79	1.52
Co	0.45	0.15	1.35	0.44	b.d.l	–	b.d.l	–	b.d.l	–	b.d.l	–
Metal												
EPMA wt%	*Na=6*	*1σ*	*Na=1*	*1σ*	*Na=3*	*1σ*	*Na=3*	*1σ*	*Na=3*	*1σ*	*Na=3*	*1σ*
Si	0.05	0.05	7.82	0.24	1.39	0.08	4.30	0.11	4.98	0.34	4.75	0.32
Ti	0.00	0.01	0.00	0.00	0.02	0.01	0.03	0.01	0.00	0.00	0.00	0.00
Al	na	na	n.a.	–	n.a.	–	n.a.	–	n.a.	–	n.a.	–
Cr	0.03	0.05	1.39	0.23	0.29	0.18	0.88	0.37	0.37	0.19	0.58	0.26
Fe	89.70	4.32	78.56	1.09	87.25	1.45	80.94	0.13	85.03	3.31	84.21	2.22
Mn	0.02	0.03	0.00	0.00	0.01	0.01	b.d.l	–	0.01	0.01	0.03	0.03
Mg	0.02	0.04	b.d.l	–	b.d.l	–	b.d.l	–	b.d.l	–	b.d.l	–
Ca	0.01	0.02	0.00	0.00	b.d.l	–	b.d.l	–	b.d.l	–	b.d.l	–
Ni	0.22	0.08	7.46	0.21	5.17	1.70	7.50	0.18	7.17	3.12	7.48	1.72
S	0.31	0.15	0.08	0.08	1.04	0.20	1.35	0.97	0.28	0.27	0.45	0.41
O	n.a.	–	n.a.	–	n.a.	–	n.a.	–	n.a.	–	n.a.	–
Total	91.3	4.1	99.9	–	95.5	0.5	95.3	1.2	100.1	0.1	100.0	0.0

(*continued on next page*)

Table 2 (*continued*)

Run	YO43-2		FM165		FM161		FM167		FM153		FM152	
ΔIW	−4.8		−5.5		−5.6		−5.5		−5.4		−5.3	
P(GPa)/T(K)	0.1	1793	0.0001	1673	0.0001	1573	0.0001	1623	0.0001	1623	0.0001	1623
LA-ICPMS ppm	*Na=3*	*1σ*	*Na=3*	*1σ*	*Na=2*	*1σ*	*Na=2*	*1σ*	*Na=2*	*1σ*	*Na=2*	*1σ*
Ni	2423	438	63,855	9873	46,621	9598	72,812	488	51,645	3163	80,388	20,400
Co	1804	80	2 775.38	303.6	2 388.37	367.06	3 401.52	22.05	2 664.94	515.75	937.33	562.42
Sulfide												
EPMA wt%	*Na=11*	*1σ*	*Na=4*	*1σ*	*Na=4*	*1σ*	*Na=3*	*1σ*	*Na=3*	*1σ*	*Na=2*	*1σ*
Si	0.02	0.06	3.24	0.03	0.02	0.01	0.02	0.01	0.02	0.00	0.01	0.00
Ti	0.12	0.12	0.74	0.02	1.00	0.43	1.74	0.70	2.00	0.24	0.26	0.11
Al	0.02	0.05	n.a	–	n.a	–	n.a	–	n.a	–	n.a	–
Cr	63.94	4.57	14.31	3.44	3.91	0.89	3.82	0.49	6.62	1.32	3.84	0.30
Fe	1.25	0.69	9.52	1.95	53.93	1.98	51.69	1.09	51.32	1.47	57.16	0.63
Mn	0.47	0.21	13.34	0.51	2.00	0.70	1.46	0.28	1.09	0.14	1.29	0.00
Mg	0.13	0.10	9.36	0.88	0.13	0.12	0.06	0.03	0.05	0.02	0.08	0.01
Ca	0.01	0.02	2.73	0.10	0.19	0.27	0.05	0.04	0.02	0.01	0.02	0.01
Ni	0.05	0.08	0.16	0.05	0.86	0.45	1.39	0.20	0.56	0.22	0.22	0.04
S	33.01	3.72	36.19	0.49	36.98	0.68	36.00	0.36	37.26	0.55	36.32	0.09
O	n.a.	–	n.a	–	n.a	–	n.a	–	n.a	–	n.a	–
Total	99.84	1.94	100.00	0.00	99.02	0.49	96.23	0.04	100.00	0.00	100.00	0.00
LA-ICPMS ppm	*Na=7*	*1σ*										
Ni	458	174	n.a	–	17 976.84	3 938.85	28 318.82	0.32	5 735.34	2.14	1 028.78	1.65
Co	291	92	n.a	–	654.77	113.38	1 333.93	0.33	281.94	2.39	45.85	1.85

was estimated according to oxide stoichiometry. Standards used were natural minerals and synthetic oxides for silicates (Si and Ca, wollastonite; Mg, forsterite; Al, Al_2O_3; Fe, fayalite; Na, albite; K, orthoclase; Ti and Mn, $MnTiO_3$; Cr, Cr_2O_3; Ni, NiO), pyrite for sulfur, pure metals (Fe, Mn, Si, Ni, Cr) for metallic alloys, and andradite ($Ca_3Fe_2Si_3O_{12}$) for oxygen. Piston-cylinder and IHPV experiments were imaged with the FEI QEMSCAN 650F scanning electron microscope (SEM) at the Faculty of Georesources and Material Engineering at RWTH Aachen (Germany) and analyzed using a JEOL JXA-8530F electron miroprobe at the University of Münster (Germany) operating with a 15 kV accelerating voltage and 10nA beam current. On-peak and background analysis times were 15 s (10 s for Na, Ni, K) and 5 s, respectively, for silicate glasses, and 20 and 10 s, respectively, for metals and sulfides. Standards used were minerals (except for Cr) for silicate melts (Na, jadeite; Mg, olivine; Al, disthene; Si, hypersthene; Ni, pentlandite; P, apatite; K, sanidine; Ca, diospide; S, pyrite; Ti, rutile; Cr, Cr_2O_3; Mn, rhodonite; Fe, fayalite) and minerals or pure metals for metals and sulfides (Mg, olivine; P, apatite; Ca, diopside; S, pyrite; and Si, Ti, Cr, Fe, Mn, and Ni metals).

2.6. Ni and Co analyses by LA-ICP-MS

Ni and Co concentrations in silicate melts, metals, and sulfides (when present) were determined by laser ablation ICP-MS. For 5 GPa and EST experiments, we used an Agilent 7500-cs ICP-MS coupled with a Resonetics M−50 laser at the LMV. The laser was operated with a wavelength of 193 nm, an energy of 6 mJ, and a fulse frequency of 2 Hz. The laser spot size on the sample was 15–50 μm for silicate melts and metals, and 6–33 μm for sulfides. Ablation was performed in a pure He atmosphere for usually about 80 s. The analyte was carried to the ICP torch by a gas mixture wherein N_2 + Ar were added to the He. We used the following gas flows: He, 750 mL/min; N_2, 4 mL/min; Ar nebulizer gas, 0.88 l/min; Ar cool gas, 15 l/min; Ar auxiliary gas, 1 l/min. Plasma power was 1,350 W. For the 26 GPa, piston cylinder, and IHPV experiments, we used an ICP-QQQ 3900 Agilent ICP-MS coupled with a Teledyne 193 nm Cetac laser with a HelEx II cell at the Department of Earth and Environmental Sciences, KU Leuven (Belgium). The laser was operated under the same conditions as for the other experiments, but the laser spot size on the sample was 20–60 μm for silicate melts, metals, and sulfides. Again, ablation was performed in a pure He atmosphere for usually about 80 s. The analyte was carried to the ICP torch by a gas mixture wherein Ar was added to the He. We used the following gas flows: He, 600 mL/min; Ar nebulizer gas, 1.39 l/min; Ar cool gas, 15 l/min; Ar auxiliary gas, 1 l/min. Plasma power was 1,550 W. We used the NIST 610 glass standard (values from Gagnon et al., 2008) for signal calibration, using Si concentrations for silicate melts and Fe concentrations for metal and sulfides. The NIST 612 and BCR standard glasses were used to check for accuracy. Our measurements are in good agreement with the recommended values (Gagnon et al., 2008), with deviations always being < 20 %. Detection limits (as determined from counting statistics on the samples) were ≤ 0.5 ppm.

2.7. Oxygen fugacity calculation

The intrinsic fO_2 values of the samples were determined using the compositions of co-existing metallic alloys and silicate melts. In log units relative to IW, fO_2 is reported as:

$$\Delta IW = 2\log_{10}\frac{a_{FeO}^{sil}}{a_{Fe}^{met}} \quad (1)$$

where a_{FeO}^{sil} is the activity of FeO in the silicate melt and a_{Fe}^{met} is the activity of Fe in the metal. a_{FeO}^{sil} and a_{Fe}^{met} were approximated here as their mole fractions; calculated fO_2 values ranged from IW − 1.9 to IW − 6.4. Incorporating activities for Fe and FeO that differ from unity based on a thermodynamic model (Holzheid et al., 1997; Wade and Wood, 2005) results in calculated fO_2 values that are higher by ~ 0.5 log units, in agreement with previous studies. However, this method was not applied since activity coefficients of FeO are neither known in highly reduced systems nor at high pressures (Righter and Ghiorso, 2012). The EST experiments were theoretically buffered at C–CO at 1300 °C, 1350 °C, and 1400 °C, which is at IW − 5.8, IW − 6.1, and IW − 6.4, respectively (fO_2 calculated with NIST-JANAF thermodynamic tables; see Supplementary Materials). In comparison, the fO_2 values calculated for the EST experiments using Eq. (1) were between IW − 5.3 and IW − 5.6 (Table 1). We therefore consider an error of ± 1 log unit on the fO_2 values calculated using Equation (1). Despite the significant error on the absolute fO_2 values, calculating fO_2 using the same method for all experiments allows us to build an internally consistent database and investigate the influence of relative fO_2 on elemental partitioning, as well as investigate the fO_2 values of planetary materials. Hence, in the following, we recalculated the fO_2 values for all compiled literature experiments using the same method.

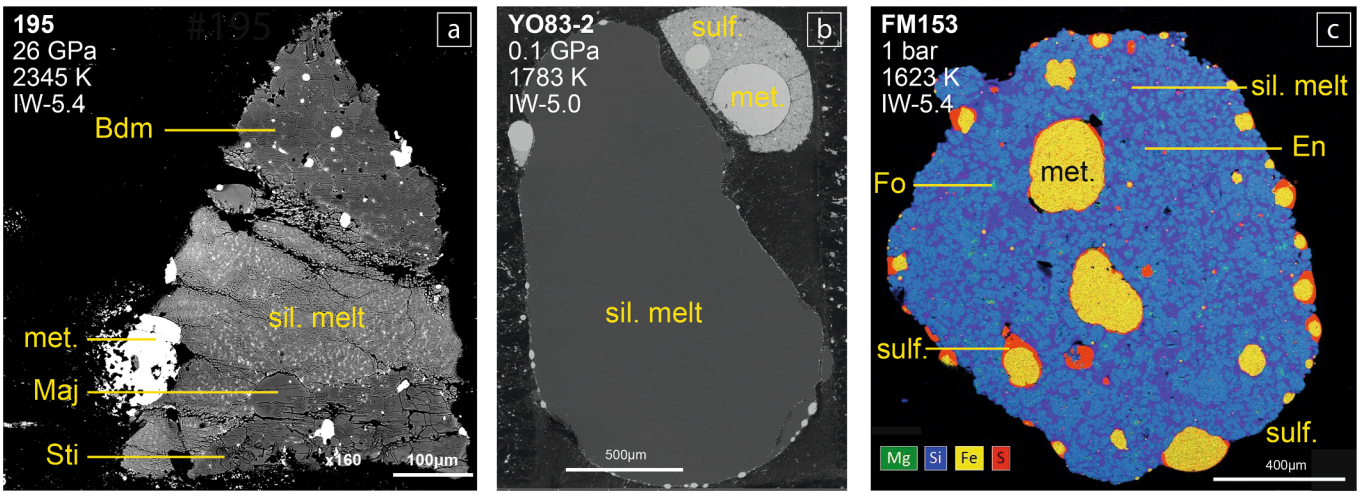

Fig. 1. (a, b) BSE images and (c) an EDS chemical map of three typical samples. Abbreviations: Bdm, bridgmanite; sil. melt, silicate melt; Maj, majorite; Sti, stishovite; met., metal; sulf., sulfide; En, enstatite; Fo, forsterite.

3. Results

3.1. Compositions of the experimental products

Each experiment contained at least a silicate melt and a metal phase, but most contained additional phases (sulfide, enstatite, forsterite, quartz, coesite, stishovite, majorite, bridgmanite) depending on the starting composition and the *P* and *T* conditions (Table 1). Representative samples obtained at various pressures are presented in Fig. 1.

All experiments contained at least one metal bead in contact with the silicate melt (Fig. 1). When present, most sulfides coated the metal beads (Fig. 1b, c). Silicate crystals displayed euhedral textures. Along with the homogeneity of the chemical compositions of the various phases throughout each sample, these textures attest that chemical equilibrium was attained. All silicate melts were quenched to glass except in the 26 GPa experiments, in which dendritic crystals formed (Fig. 1a).

Silicate melts were roughly chondritic in composition, with the ratio of non-bridging oxygens to tetrahedrally coordinated network former cations (Mysen, 1983) ranging from 0.7 to 2.5 and FeO contents from 0.03 to 12.9 wt%, corresponding to fO_2 from IW − 6.4 to IW − 1.9 (Tables 1 and 2). They contained 0–12.5 wt% sulfur, which strongly depended on temperature and fO_2; i.e. more reduced and hotter experiments contained more sulfur (Namur et al., 2016; Fig. 2). Metallic melts were dominated by Fe or alloyed with 0–42.6 wt% Si, also strongly depending on temperature and fO_2 (Kilburn and Wood, 1997; Fig. 2). Due to the large miscibility gap in Fe-S-Si systems at ≤ 5 GPa (Morard and Katsura, 2010), most experiments conducted in this pressure range contained enough S to produce two alloys, the previously mentioned 'metallic' alloy and a FeS-dominated melt that we will call 'sulfide' hereafter (Fig. 1b, c). Hence, experiments performed at ≤ 5 GPa contained metals with 0.01–5.75 wt% S, and the highest S contents corresponded to metals containing negligible Si in the most oxidizing experiments (Fig. 2). Consistent with the lack of immiscibility in the Fe-Si-S system 26 GPa (Morard and Katsura, 2010), our experiments at 26 GPa contained a single metallic phase dominated by Fe and containing 0.01–23.07 wt% Si and 6.65–36.02 wt% S, the composition of which again strongly depending on temperature and fO_2 (Fig. 2). A few 26 GPa experiments were contaminated by La and Cr diffusing from the $LaCrO_3$ furnace at high *P-T* conditions (Table 2); therefore, some metals contained high amounts of Cr (up to 27.04 wt% Cr in the metal phase of sample #143), and some silicate melts contained high La concentrations (up to 4.28 wt% La in the silicate melt of sample #143). Nonetheless, these contaminated experiments were fully equilibrated and show Ni and Co partitioning results consistent with those from non-contaminated

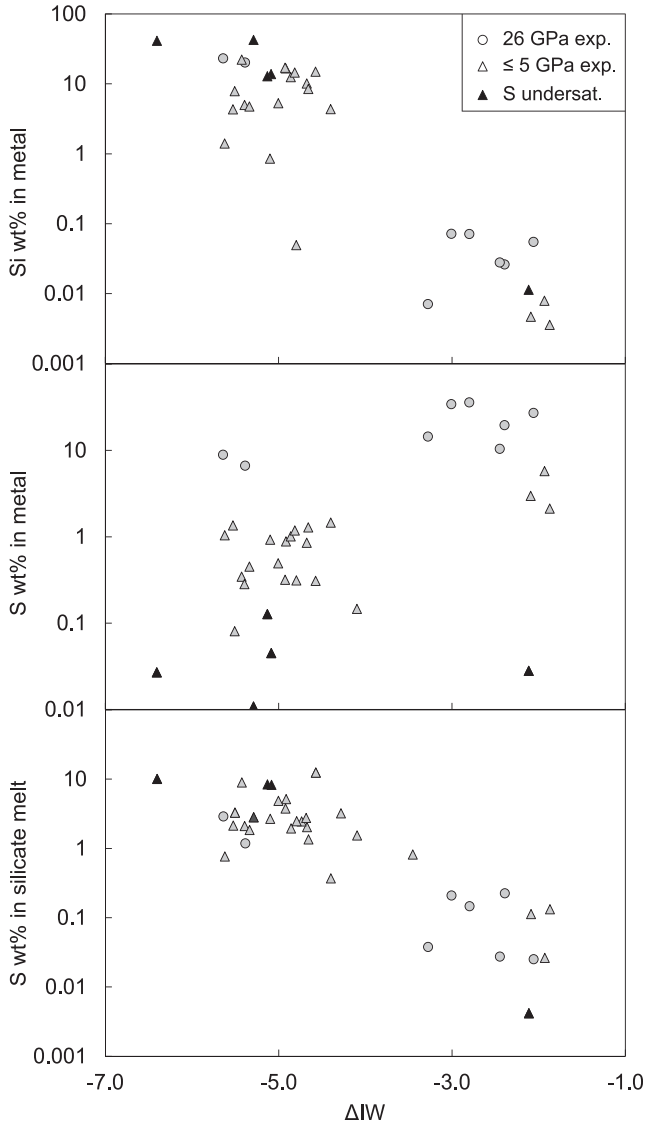

Fig. 2. Metal and silicate compositions of the experiments. Circles, 26 GPa experiments; triangles, 5 GPa and lower pressure experiments. Black symbols indicate sulfide-undersaturated experiments.

experiments conducted under similar conditions. Sulfides were present in most ≤ 5 GPa experiments and were dominated by an FeS component, except those in the most reduced experiments that contained up to 22.4 wt% Mg, 14.3 wt% Cr, 5.9 wt% Mn, 2.7 wt% Ca, and 2.0 wt% Ti; these abundances of these elements in sulfides are strongly anticorrelated with fO_2 (Fig. S1).

3.2. Ni and Co metal–silicate partition coefficients

Based on our experimental results, we calculated Ni and Co metal–silicate partition coefficients as D_{Ni} = (wt% Ni in metal)/(wt% Ni in silicate melt) and D_{Co} = (wt% Co in metal)/(wt% Co in silicate melt). Along with our values, we compiled literature data (Thibault and Walters, 1995; Hillgren et al., 1996; Jana and Walker, 1997; Righter et al., 1997, 2010; Gaetani and Grove, 1997; Gessmann and Rubie, 1998; Wade and Wood, 2001, 2005; Bouhifd and Jephcoat, 2003, 2011; Asahara et al., 2004; Chabot et al., 2005; Kegler, 2008; Corgne et al., 2008; Mann et al., 2009; Wood et al., 2009; Siebert et al., 2011, 2012, 2013; Bouhifd et al., 2013; Cartier et al., 2014a, 2014b; Righter, 2015; Fischer et al., 2015; Huang and Badro, 2018; Steenstra et al., 2020a, 2020b) to build a database of 315 experiments corresponding to 251 D_{Ni} and 194 D_{Co} values and covering a wide range of pressures (1 bar to 100 GPa), oxygen fugacities (IW − 6.4 to IW + 0.2), and temperatures (1573–5700 K) (Fig. 3, Table S7), and for which fO_2 and the Ni and Co partition coefficients were calculated using the same method as for our experiments. D_{Ni} and D_{Co} are very strongly negatively correlated with fO_2, and strongly negatively correlated with P and T (Fig. 3). Our new data, which mainly fill the fO_2 gap between IW − 6.4 and IW − 4, define a linear relationship when plotted as a function of fO_2 and continue the trend from data obtained at higher fO_2 (Fig. 3a, b). In 1 bar experiments, D_{Ni} ranges from ~ 3×10^2 at IW to ~ 3×10^5 at IW − 6, and D_{Co} from ~ 15 at IW to ~ 5.5×10^3 at IW − 6. The negative linear correlation between log(D) and fO_2 is predicted by the thermodynamics of Ni and Co chemical exchange between metal and silicate melts (Wade and Wood, 2005). Furthermore, the absence of any break in slope is consistent with Ni and Co dissolving in silicate melts as NiO and CoO species over the entire fO_2 range. Likewise, Ni and Co become less siderophile with increasing pressure (Fig. 3c, d). In IW − 1 experiments, D_{Ni} ranges from ~ 10^3 at 1 bar to ~ 10 at 60 GPa, and D_{Co} from ~ 10^2 at 1 bar to ~ 5 at 60 GPa. Above 60 GPa, the pressure effect becomes negligible, as previously described by Bouhifd and Jephcoat (2003). Similarly, Ni and Co become less siderophile with increasing temperature (Fig. 3d, e). However, the relative effects of pressure and temperature are not independent, making them difficult to visualize; this will be developed in Section 3.3. Globally we observe that, as a result of the combined effects of P, T, and fO_2, Ni is more siderophile than Co under most conditions, except when Co becomes more siderophile at high pressure and low fO_2 (above ~ 40 GPa at IW − 3 and above ~ 30 GPa at IW − 5).

Previous results on the effects of silicate and metal compositions on Ni and Co metal–silicate partitioning have been contradictory (Fischer et al., 2015; Righter, 2015; Huang and Badro, 2018). Our database includes experiments spanning a large compositional range, with NBO/T values ranging from 0.5 to 4.7 (Tables 1, S7). Fig. 4a, b shows no clear correlation between logD_{Ni} or logD_{Co} and NBO/T. Our database also includes experiments spanning a large range of metal compositions, with sulfur contents X_S (mole fraction) ranging from 0 to 0.52; similarly, Fig. 4c, d shows no obvious correlation between partition coefficients and X_S. Therefore, D_{Ni} and D_{Co} are not significantly affected by silicate melt and metal compositions, as will be confirmed by statistical tests presented in Section 3.3.

3.3. Parameterizing Ni and Co metal–silicate partition coefficients

D_{Ni} and D_{Co} are strongly correlated with fO_2, P, and T (Fig. 3). We therefore parameterized the experimental D_{Ni} and D_{Co} values as a function of those three parameters following a similar formalism as used in previous studies (Wade and Wood, 2005; Fischer et al., 2015; Righter, 2015) and using Eq. (2) (noting that in Fischer et al. (2015), fO_2 was not directly fitted as a parameter but was integrated into the Ni–Fe and Co–Fe exchange coefficients, themselves fitted as functions of P and T):

$$\ln D = a + b(\mathrm{IW}) + c\frac{1}{T} + d\frac{P}{T} \quad (2)$$

Fitting parameters a–d are reported in Table 3. We obtained good fits with R^2 values of 0.881 for Ni and 0.864 for Co (Fig. S2). D_{Ni} is more strongly dependent on pressure and temperature than D_{Co}, and D_{Ni} and D_{Co} both have a similar fO_2 dependencies (Table 3), as previously reported by Righter (2015) and Fischer et al. (2015). We explored the influence of NBO/T on Ni and Co partition coefficients, but found no statistically significant correlation ($p = 0.1$ for Ni and $p = 0.05$ for Co), in agreement with the results of Fischer et al. (2015) and Huang and Badro (2018). We also investigated the influence of metal sulfur content; however, contrary to Righter (2015), we found that the correlation between the partition coefficients and X_S is statistically insignificant (p = 0.2 for Ni and p = 0.2 for Co). This model can confidently be used to predict D_{Ni} and D_{Co} over the range of 1 bar to 80 GPa and IW − 6 to IW.

Our results are very similar to those of Fischer et al. (2015) for Ni and Co concerning the effect of pressure, whereas Righter (2015) found a more pronounced effect of P on D_{Ni} (Fig. 5). We observe the effects of fO_2 on both D_{Ni} and D_{Co} to be weaker than reported by Fischer et al. (2015), but slightly more pronounced than reported by Righter (2015).

3.4 Ni and Co sulfide–silicate partition coefficients

Using our sulfide-saturated experiments, we calculated Ni and Co sulfide–silicate melt partition coefficients as $D_{Ni}^{sulf/sil}$ = (wt% Ni in sulfide)/(wt% Ni in silicate melt) and $D_{Co}^{sulf/sil}$ = (wt% Co in sulfide)/(wt% Co in silicate melt) (Table 2). Alongisde the experiments of Steenstra et al., (2020b), our results show that Ni and Co sulfide–silicate partition coefficients follow the same P, T, and fO_2 dependencies as the metal–silicate partition coefficients, but with D values roughly 10 and 5 times lower for Ni and Co, respectively (Fig. S3).

4. Discussion

4.1. Modeling Ni and Co $D^{met/sil}$ along the liquidus of a chondritic mantle

Using our parameterization, we model Ni and Co $D^{met/sil}$ values along the liquidus of a chondritic mantle (Herzberg and Zhang, 1996; Andrault et al., 2011) (Fig. S4) at various P and fO_2 conditions covering the range of 1 bar to 80 GPa and IW − 6 to IW. The fO_2 and P dependencies of D_{Ni} and D_{Co} displayed by the experimental data is very well reproduced by our model (Fig. S5). We then plot these models in D_{Ni} *vs.* D_{Co} space over the considered P and fO_2 ranges (Fig. 6). Hypothesizing that in planetary bodies, metal–silicate equilibrium is attained in magma oceans at liquidus temperatures, plotting the bulk core–bulk silicate Ni and Co partition coefficients in this pseudo P–fO_2 space gives insights into the pressure and redox conditions at which a given body differentiated. Finally, as our model integrates S-bearing systems, any terrestrial body can be investigated, including those likely to contain not just a metallic, but also a sulfide component in their core (e.g., Mercury; Cartier et al., 2020; Pirotte et al., 2023) because their differentiation occurred at low enough pressures for Fe(Si) and FeS melts to be immiscible (Morard and Katsura, 2010). Indeed, compared to the metal phase, the formation of such a sulfide phase during core formation would have a negligible effect on the primitive mantle Ni and Co contents because Ni and Co sulfide–silicate partition coefficients are 5–10 times lower than their metal–silicate partition coefficients under all P–fO_2 conditions covered by our model (see Section 3.4).

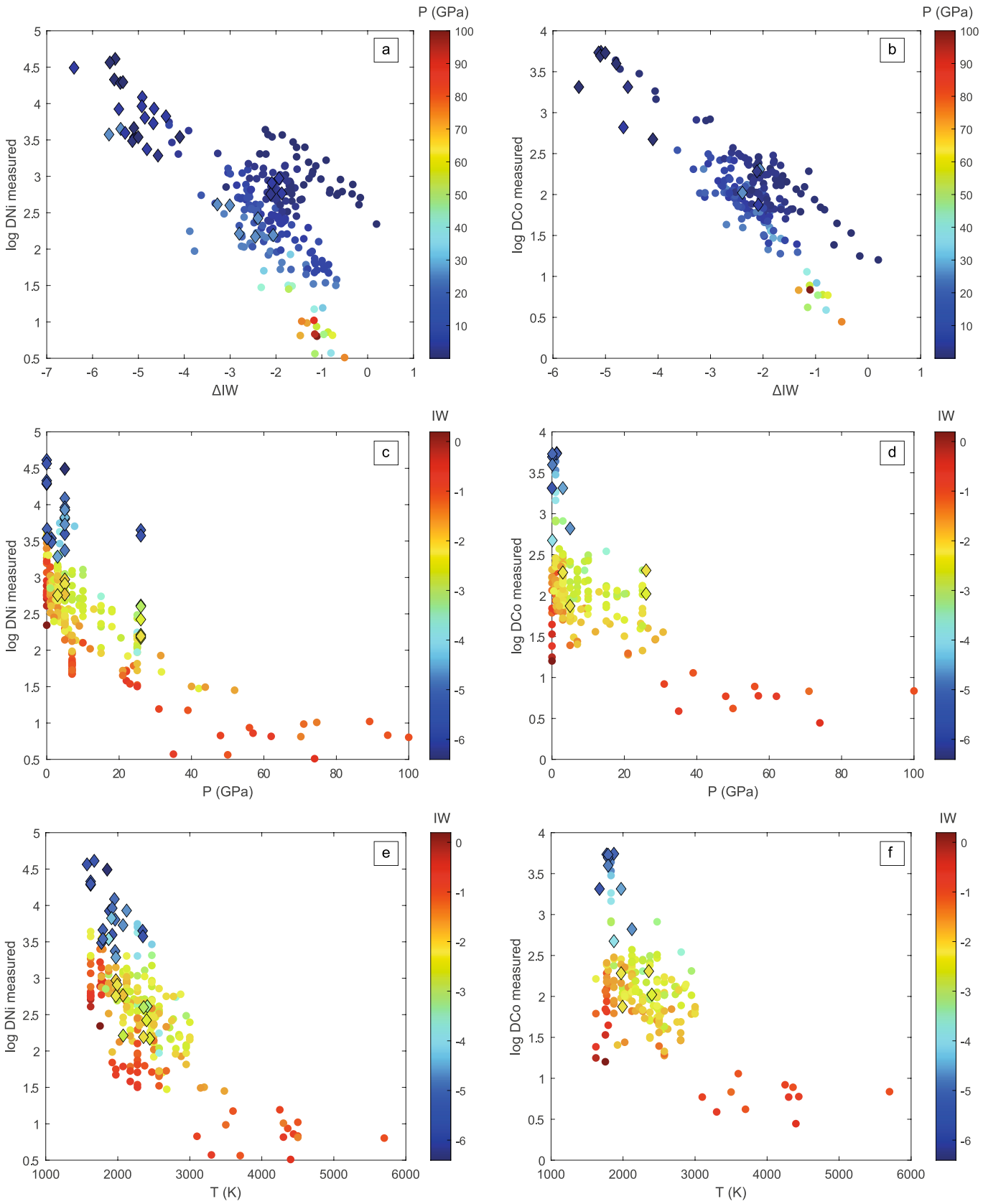

Fig. 3. Ni and Co metal–silicate partition coefficients of experiments conducted in various chemical systems at various P, T, and fO_2 conditions (Table 2; prior data provided in Table S7) plotted as functions of (a, b) fO_2 relative to IW, (c, d) pressure, and (e, f) temperature. New data from this study are plotted as diamonds.

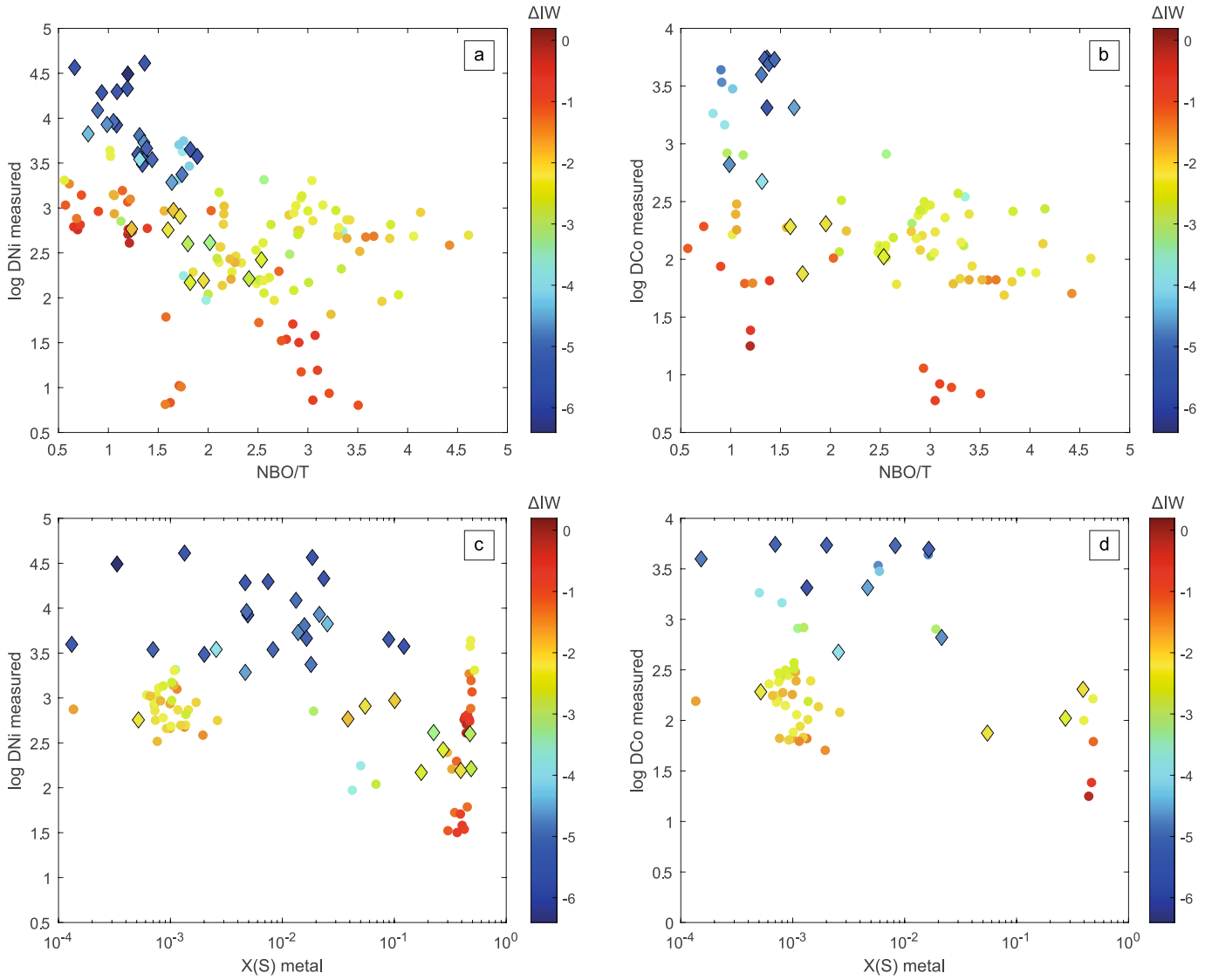

Fig. 4. Ni and Co metal–silicate partition coefficients of experiments conducted in various chemical systems at various P, T, and fO_2 conditions (Table 2; prior data provided in Table S7) plotted as functions of (a, b) NBO/T and (c, d) X_S, the molar fraction of sulfur in the metal. New data from this study are plotted as diamonds.

Table 3
Parameters obtained by regression of the experimental database with Eq. (2). Standard errors for the individual terms are in parentheses.

	a	*b*	*c* (1/K)	*d* (GPa/K)	R^2	*p*-value, *b*	*p*-value, *c*	*p*-value, *d*
Ni	1.70 (0.32)	−0.796 (0.032)	6815 (616)	−147 (12)	0.881	4E-69	2E-23	5E-26
Co	1.16 (0.33)	−1.019 (0.039)	3573 (638)	−87 (14)	0.864	2E-65	8E-08	2E-09

4.2. Application to Earth, Mars, the Moon, and Vesta

Earth and Mars (the parent body of Shergottite, Nakhlite, and Chassignite—SNC—meteorites) have well constrained bulk silicate and bulk core compositions (Dreibus and Wänke, 1980; McDonough and Sun, 1995; Lodders and Fegley, 1998; Taylor, 2013; Palme and O'Neill, 2014). In contrast, the compositions of the Moon and Vesta (the parent body of Howardite, Eucrite, and Diogenite—HED—meteorites) are much less constrained, although a variety of models exist for their silicate portions and cores (Dreibus and Wänke, 1980; Delano, 1986; Steenstra, 2016). Table 4 presents selected values of Ni and Co contents of the bulk silicate and bulk core portions of these four terrestrial bodies, with corresponding calculated bulk core–bulk silicate Ni and Co partition coefficients.

The bulk silicate portions of Earth, Mars, the Moon, and Vesta have been estimated in previous studies (Table 4) following a cosmochemical formalism that we develop here. Fig. 7 shows a compilation of bulk rock Ni and Co analyses of rocks and meteorites originating from Earth, Mars, the Moon, and Vesta, plotted as a function of Mg/Al and compared with their respective parent bodies' bulk silicate values from Table 4. Planetary differentiation is the result of early, protracted processes: the formation of a metal core during a magma ocean stage, the crystallization of the silicate portion to generate a primitive crust, and the later melting of the mantle to generate a secondary crust. All the rocks making up the silicate fraction of a planet, from the most primitive mantle rocks to the most evolved crustal rocks, are therefore linked to their parent reservoir (i.e. the bulk silicate portion of the planet) by a combination of crystallization, melting, mechanical sorting, and mixing processes

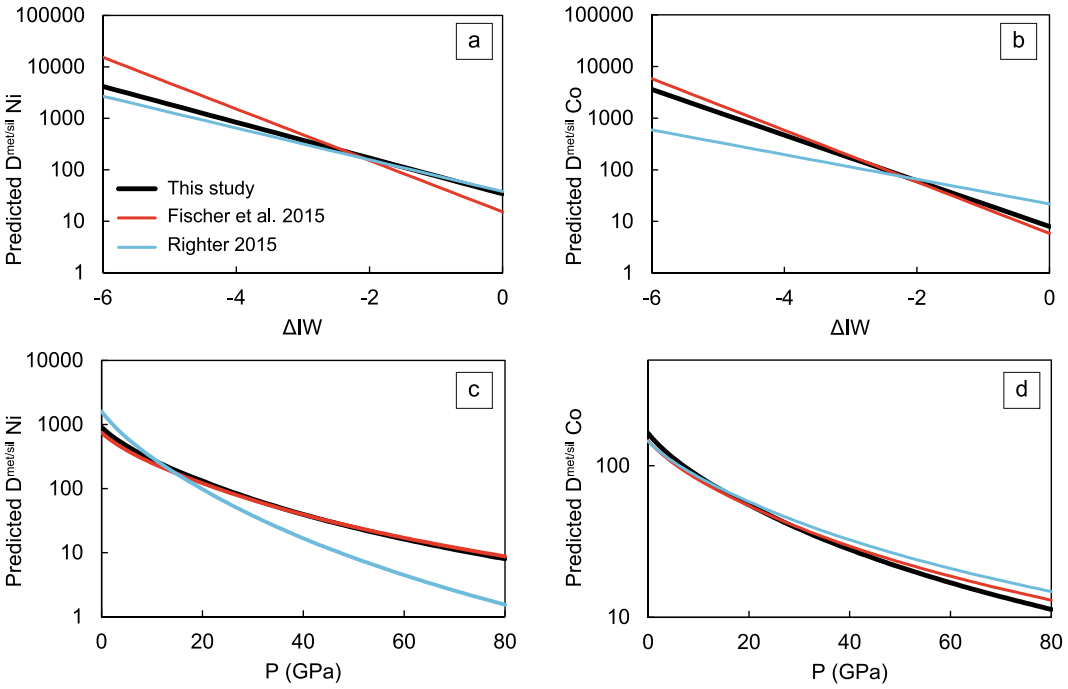

Fig. 5. Comparison of the predictive models of Ni and Co metal–silicate partitioning from Righter (2015), Fischer et al. (2015), and this study. (a, b) Model results at a fixed pressure (15 GPa) and temperature (2472 K), displayed as a function of fO_2. (c, d) Model results at a fixed fO_2 of IW − 2.1 and chondritic liquidus temperatures (Andrault et al., 2011; Herzberg and Zhang, 1996), displayed as a function of pressure. Righter's (2015) model was run with a sulfur- and carbon-free metal composition and silicate NBO/T = 2.49.

(Palme and O'Neill, 2014). The compositions of terrestrial igneous, mantellic, and crustal rocks (from the GEOROC database, https://georoc.eu/), when plotted for a given element as a function of Mg/Al, reveal a continuous trend whose shape indicates the main phases controlling that element's fractionation during magmatic processes (Fig. 7; Palme and O'Neill, 2014).

Assuming that the bulk silicate Earth has chondritic refractory lithophile element (RLE) ratios (e.g., Mg/Al = 8–13; Lodders and Fegley, 1998; Palme and O'Neill, 2014), the intersection of the trends with the chondritic RLE range gives the composition of the bulk silicate Earth (Fig. 7; McDonough and Sun, 1995; Palme and O'Neill, 2014). For other terrestrial bodies for which we have sufficient data, a similar approach can be used to calculate their bulk silicate compositions. The bulk Ni and Co contents of silicate rocks from Mars (as sampled by SNC meteorites (MetBase database, https://metbase.org/) and surface rocks (Yen et al., 2006)), the Moon (as sampled by surface rocks and regolith (Lunar Sample Compendium database,; Lodders and Fegley, 1998) and lunar meteorites (MetBase)), and Vesta (as sampled by HED meteorites; MetBase) align along continuous trends (Fig. 7), although the data are particularly scattered for Vesta and the Moon due to regolith contamination by the late accretion of chondritic material (Wang et al., 2023). The intersections of these trends and the chondritic Mg/Al range matches their bulk silicate compositions (Fig. 7). Each bulk silicate Ni and Co content is strongly subchondritic, indicating the depletion of siderophile elements during core formation because neither element is volatile and they are therefore unaffected by devolatilization processes (Lodders, 2003). In Section 4.3, we will use this method to estimate the Ni and Co contents of the silicate portions of less constrained planetary bodies.

Our modeling results based on D_{Ni} and D_{Co} (Fig. 6, Table 4) indicate the P–fO_2 conditions for the magma oceans of Earth, Mars, the Moon, and Vesta to be IW − 2.2 and 50 GPa, IW − 1.3 and 6 GPa, IW − 1.2 and 1 GPa, and IW − 2.2 and < 1 bar, respectively (Table 5). To test the influence of the assumed liquidus temperature on the results, we calculated two adiabats, one hotter than the liquidus (+160 °C at 1 bar, +249 °C at 80 GPa) and one cooler than liquidus (i.e., corresponding to the 50 % melting curve; −160 °C at 1 bar, −249 °C at 80 GPa) (Fig. S4), which we input into our model to compare with the results obtained using the liquidus (Fig. S6). The largest difference between the three models is 2 GPa and 0.1 log unit fO_2, far smaller than the errors induced by the uncertainties on planetary D_{Ni} and D_{Co} values (Fig. S6, Table S8). We therefore conclude that modeling D_{Ni} and D_{Co} along a peridotitic/chondritic liquidus is adequate, even if the planetary bodies had hotter or cooler adiabats than those of the Earth or Mars.

Our results for Earth and Mars are in excellent agreement with both the fO_2 and pressure conditions estimated for core formation using MSE abundances (including Ni and Co) in their silicate portions (Righter and Drake, 1997; Wade and Wood, 2005; Wood et al., 2009; Righter and Chabot, 2011; Rubie et al., 2011; Mandler and Elkins-Tanton, 2013; Fischer et al., 2015; Righter, 2015), as well as fO_2 estimations based on independent methods (e.g., XANES; Righter et al., 2016). Concerning the Moon, Righter and Drake (1996) and Steenstra et al. (2016) estimated pressures of 3.5 and 4–5 GPa based on MSE abundances in the lunar mantle; we obtained a lower pressure of 1 GPa, but the error bars overlap. Our fO_2 result for the Moon matches their results, as well as the fO_2 measured in lunar rocks (Righter et al., 2016). Finally, Righter and Drake (1996) estimated ≤ 1 bar and IW − 2.2 for Vesta, the HED parent body, and our results are identical.

The pressure thusly obtained for Earth (50 GPa) corresponds to 37 % that at its CMB (135 GPa), and that for Mars (6 GPa) to 25 % that at its CMB (24 GPa). The pressure obtained for the Moon (1 GPa) corresponds to 22 % that at its CMB (4.5 GPa; Briaud et al., 2023) very similar to the Moon and Mars; however, this result is surprising because the Moon did not form by the accretion of chondritic-like material, as did Earth and Mars. Finally, pressure obtained for Vesta (<1 bar) is significantly lower than the CMB pressure estimated for Vesta (1,000–2,000 bars; Lenhart and Secco, 2022). Overall, these results correlate with parent body size (Fig. 8); plotting Vesta and the Moon alongside Earth and Mars produces an excellent polynomial curve, attesting to the robustness of this method. This suggests that we can similarly unravel the thermodynamic

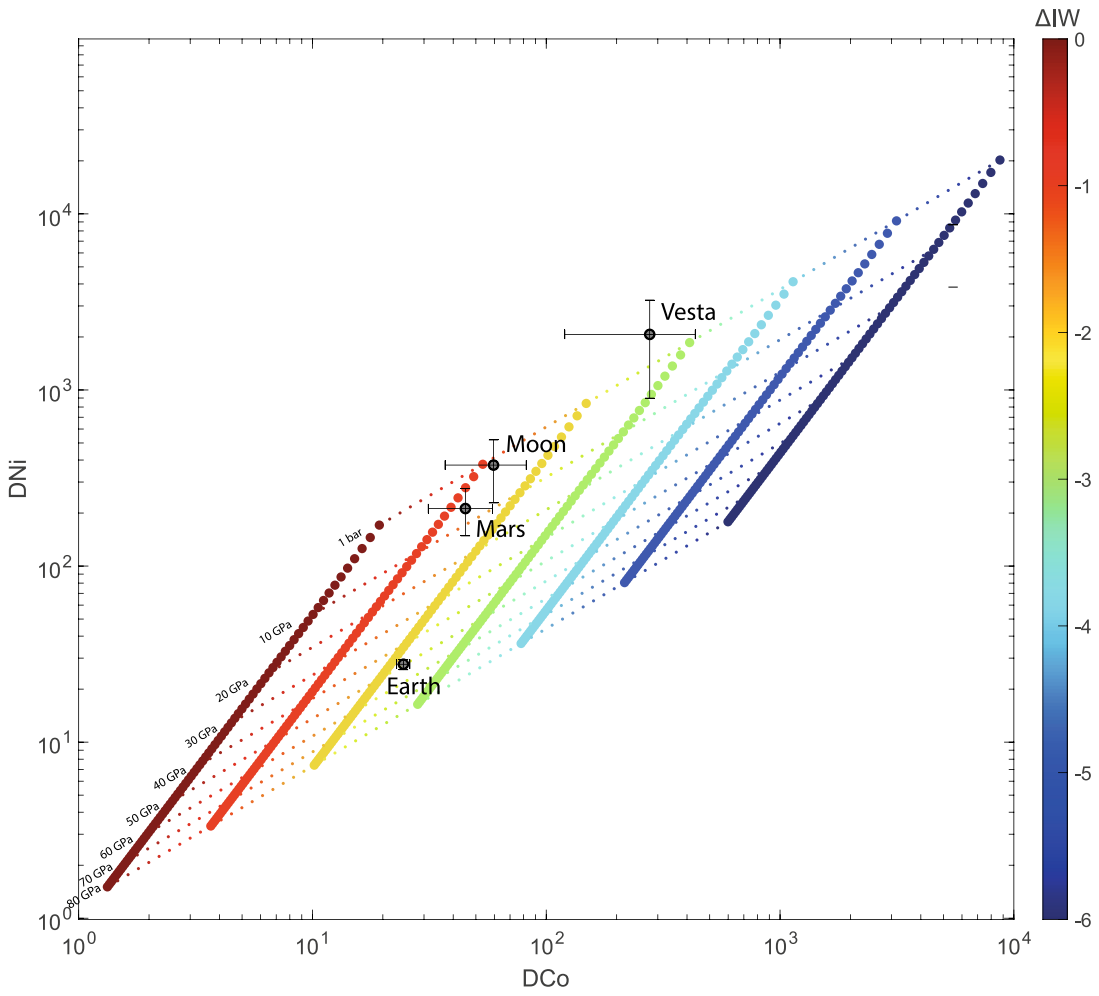

Fig. 6. Pseudo P–fO_2 space (GPa *vs.* ΔIW) drawn by modeling Ni and Co $D^{met/sil}$ values along the liquidus of a chondritic mantle. Core–mantle Ni and Co $D^{met/sil}$ values calculated for Earth, Mars, the Moon, and Vesta are plotted to retrieve the prevailing thermodynamic conditions during their core formation: 50 GPa and IW − 2.2 for Earth, 6 GPa and IW − 1.3 for Mars, 1 GPa and IW − 1.2 for the Moon, and < 1 bar and IW − 2.2 for Vesta. The intersections of the error bars and the P–fO_2 grid give maximum and minimum P and fO_2 values, and thus an estimate of their associated errors.

Table 4
Selected values for the Ni and Co contents of the bulk silicate and bulk core portions of Earth, Mars, the Moon, and Vesta. References: [1], Palme and O'Neill (2014); [2], McDonough and Sun (1995); [3], Taylor (2013); [4], Righter and Drake (1996); [5], Delano (1986); [6], Steenstra (2016); [7], Dreibus and Wänke (1980).

	Bulk silicate					Bulk core					Partition coefficients			
	Reference	Ni %	σ	Co ppm	σ	Reference	Ni %	σ	Co ppm	σ	Ni	σ	Co	σ
Earth	[1]	0.186	0.009	102	5	[2]	5.2	0.3	2500	100	28	2	25	2
Mars / SNC	[3]	0.033	0.005	71	13	[4]	7.0	1.8	3200	800	212	64	45	14
Moon / Lunar met.	[5]	0.047	0.005	90	5	[6]	17.6	6.6	5355	208	374	146	60	23
Vesta / HED	[7]	0.0038	0.0015	13	5	[7]	7.9	3.1	3600	1440	2068	1170	277	157

conditions of other terrestrial bodies as long as we can estimate their bulk Ni and Co partition coefficients. Alternatively, our model could also be applied to any object containing silicate melt and metal at equilibrium, such as chondrules (van Kooten et al., 2022) or individual achondrites (Ray et al., 2021), by measuring *in-situ* Ni and Co partition coefficients.

4.3. Application to other achondrite parent bodies

Angrites, aubrites, the paired ungrouped achondrites NWA 7325, NWA 8486, and NWA 8409, the paired ungrouped achondrites NWA 011 and NWA 2976, and the ungrouped achondrite Erg Chech 002 form five groups of achondrites, each derived from one or more parent bodies whose properties, particularly sizes, remain controversial or unknown (Yamaguchi et al., 2002, 2021; Isa et al., 2008; Irving et al., 2013; Mittlefehldt, 2014; Barrat et al., 2015, 2021; Weber et al., 2015; Frossard et al., 2019; Nicklas et al., 2022). The five achondrite families are considered to be of asteroidal origin, some sharing spectral properties with specific asteroid families (Mittlefehldt, 2014; DeMeo et al., 2022). However, even if such parenthood is proven, as for aubrites and E-type asteroids (Gaffey et al., 1992; Fornasier et al., 2008), information on the size of the original parent body is still lacking because most asteroids are rubble piles, reassembled pieces of precursor parent bodies (Delbo et al., 2017). All these meteorites are unambiguously differentiated achondrites, i.e. they crystallized from a melt in the silicate portion of their parent body after core formation (Mittlefehldt, 2014). The

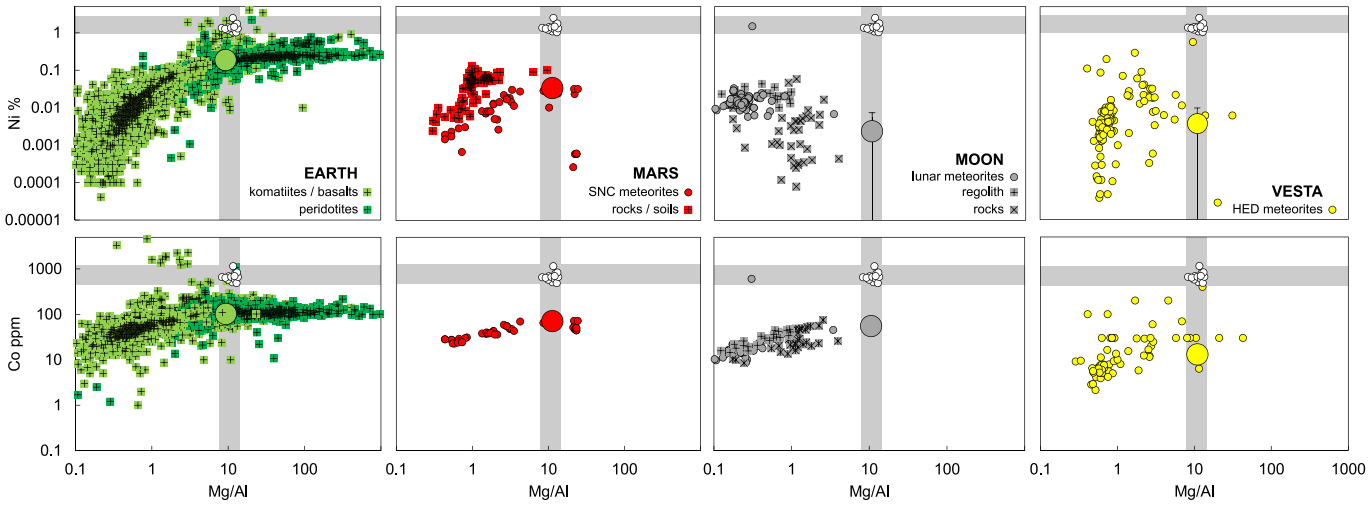

Fig. 7. Compilation of bulk rock Ni and Co contents in samples from Earth, Mars (SNC meteorites), the Moon (lunar meteorites), and Vesta (HED meteorites), compared to bulk data from chondrites (white dots; Lodders and Fegley, 1998). Each element is plotted as a function of Mg/Al. Earth komatiites, basalts, and peridotites are from GEOROC. Mars rocks and soils are from Yen et al. (2006), Moon regolith and rocks are from the Lunar Sample Compendium database, and SNC, lunar, and HED meteorites are from MetBase. The bulk silicate compositions of Earth, Mars, the Moon, and Vesta (large dots) are from Palme and O'Neill (2014), Taylor (2013), Delano (1986), and Dreibus and Wänke (1980), respectively (Table 4).

Table 5
Pressure and fO_2 results obtained by plotting planetary D(Ni) – D(Co) in the modelled pseudo P- fO_2 space (Fig. 5). Pressure and fO_2 maximum and minimum values correspond to the plot of the error bars associated with D(Ni) – D(Co); these values gives an approximate of the error on the results, e.g. the pressure obtained for Earth is 50^{+3}_{-3} GPa. Bulk silicate FeO values are from Palme et al. (2014) for Earth, Khan et al. (2022) for Mars, Elkins-Tanton et al. (2011) for the Moon, and Lodders (2000) for Vesta, respectively.

	Radius (km)	BS FeO wt%	σ	P (GPa)	P max (GPa)	P min (GPa)	fO_2 (ΔIW)	fO_2 max (ΔIW)	fO_2 min (ΔIW)
Earth	6371	8.1	1.3	50	53	47	−2.2	−2.1	−2.3
Mars	3390	13.7	0.5	6	13	2	−1.3	−0.6	−1.7
Moon	1737	12.5	4.5	1	9	< 0.0001	−1.2	−0.4	−1.8
Vesta	263	13.7	4.6	<0.0001	5	< 0.0001	−2.2	−0.7	−3.0

homogeneous oxygen isotopic compositions ($\Delta^{17}O$) of angrites and, separately, aubrites indicate that the angrite parent body (APB) and the aubrite parent body (AuPB) independently underwent large-scale melting, possibly corresponding to a magma ocean stage (Greenwood et al., 2005). Furthermore, except for samples showing clear evidence of chondritic contamination (due to late accretion and/or exogeneous contamination in the regolith; Wang et al., 2023), all these achondrites are depleted in both siderophile and chalchophile elements compared to chondrites, and the degree of depletion is homogeneous for each assumed parent body, even if there is more scatter for aubrites, as will be discussed in the following (Fig. 9). Efficient core formation in the parent bodies of angrites, aubrites, and NWA 7325/8486/8409 is further supported by several arguments, such as the Ni isotopic compositions of these meteorites (Wang et al., 2023) and the presence of melt inclusions in their minerals (Mittlefehldt, 2014). Moreover, the degrees to which siderophile elements are depleted in these five groups of achondrites mostly correlate with the degree to which each element behaves as siderophile/chalcophile, indicating that their parent bodies experienced core formation via metal–silicate or sulfide–silicate equilibrium (Lodders et al., 1993; Mittlefehldt, 2014; Goodrich et al., 2017). This theoretically allows us to use the subchondritic Ni and Co contents of all five groups of achondrites to model their parent bodies' core–mantle partition coefficients and probe the *P*–fO_2 conditions during their differentiation, whether total or partial. This treatment assumes that core formation was complete and that no relict chondritic metal/sulfide remained in the primitive mantles.

Most of the Ni and Co budgets in achondrites are carried by metal and/or sulfide phases present, on average, in trace amounts in angrites, NWA 7325/8486/8709, NWA 011/2976, and Erg Chech 002, and that account for 0.2 vol% of aubrites on average (Keil, 2010; Mittlefehldt, 2014; Goodrich et al., 2017). In the angrite and aubrite families, some samples have wt% abundances of metal phases, representing outliers anomalously enriched in Ni and Co (Fig. 9); indeed, exogeneous particles, chondritic material, or, more rarely, iron meteorite components have been identified in most of these samples (Keil, 2012; Ray et al., 2021; Zhu et al., 2022). Similarly, some metal-rich aubrite samples contain metal particles proposed to have originated from the core of the AuPB, thus having been mixed with the silicate portion during its catastrophic disruption (Van Acken et al., 2012). Excluding those outliers, each of these five achondrite families display rather homogeneous Ni and Co contents, despite important scatter for aubrites (Fig. 9). This scatter might be related to late additions/contaminations that would have artificially increased the Ni and Co contents of some samples (Wang et al., 2023), or the presence of relict metal trapped in the silicate portion of the parent body during magma ocean crystallization, as has been proposed for the origin of metal in aubrites (Casanova et al., 1993). Such processes would randomly affect samples and artificially increase the average bulk Ni and Co contents. However, the effect of this contamination should be an order of magnitude smaller than the observed Ni and Co depletions of achondrites relative to chondrites.

Therefore, we here hypothesize that, after excluding Ni- and Co-rich outliers, and as for lunar, SNC, and HED meteorites that also contain trace metal/sulfides (Dreibus and Wänke, 1980; Paquet et al., 2021; Wang et al., 2023), the Ni and Co abundances are representative of the bulk silicate portions of the parent bodies (Figs. 7 and 9). This implies that the origin of the metal and/or sulfide phases is mostly magmatic, i.e. formed by exsolution from magmas and/or subsolidus processes, as proposed for sulfides and/or metal in aubrites, SNC meteorites, and

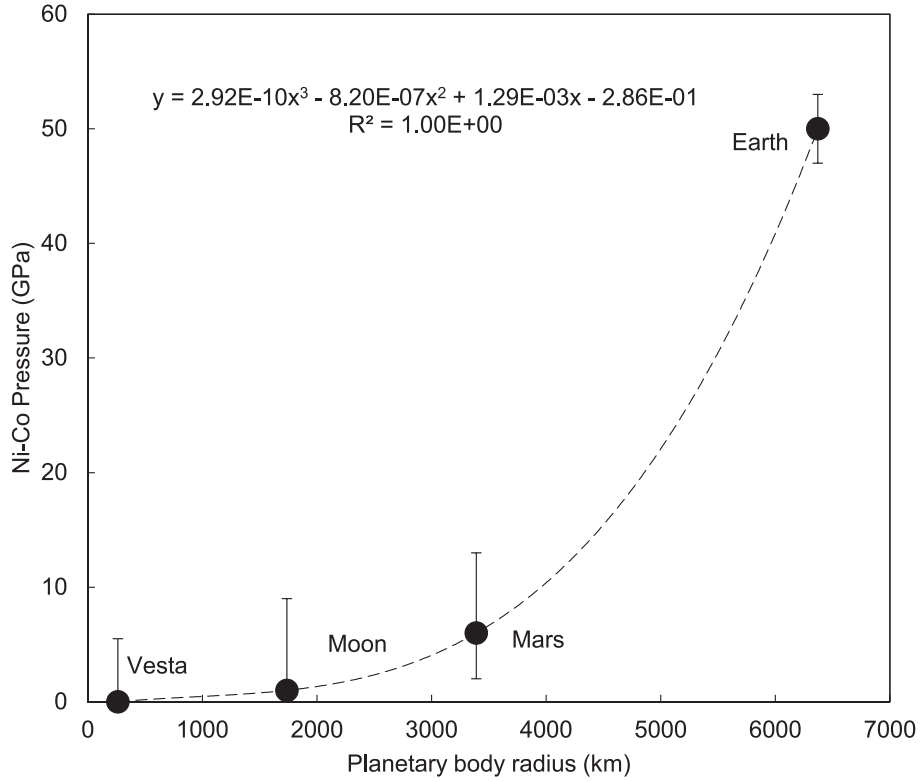

Fig. 8. Magma ocean pressures determined from Ni and Co partitioning *vs.* planetary body radius (km). Polynomial regression reveals an excellent correlation.

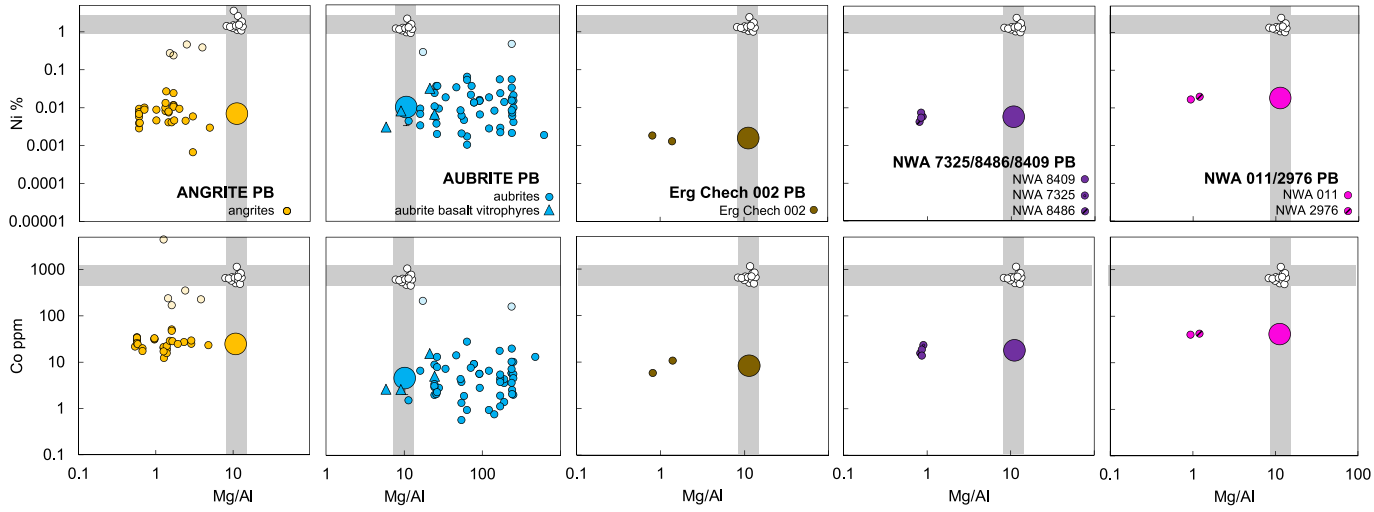

Fig. 9. Compilation of bulk rock Ni and Co contents in angrites, aubrites, Erg Chech 002, NWA 7325/8486/8409, and NWA 011/2976 compared to bulk chondrite bulk (white dots; Lodders and Fegley, 1998). Both elements are plotted as a function of Mg/Al. Most achondrite data come from MetBase, the bulk compositions of aubrite basalt vitrophyres from Fogel (2005) and Keil et al. (2011), additional data for achondrites from Wang et al. (2023), and additional data for aubrites from Wilbur et al. (2022). The large circles correspond to our estimation of the bulk silicate achondrite parent body compositions, i.e. the median values of Ni and Co data, excluding outliers (shown by semi-transparent symbols). The error bars on the bulk silicate compositions correspond to the median absolute deviation of the data. The Mg/Al ratio of the bulk silicate is fixed at 11.2 (i.e. the CI value; Lodders and Fegley, 1998) for the purposes of this figure, but not elsewhere.

angrites (McCoy, 1998; Fogel, 2005; Jambon et al., 2011; Paquet et al., 2021). In this scheme, the significant scatter among the aubrite data could simply result from heterogeneous sampling of various lithologies containing various amounts of magmatic metal/sulfides. This argument is consistent with the fact that aubrites are coarse-grained, nearly monomineralic lithologies, randomizing sampling for bulk analyses (Keil, 2010). In this scenario, then, the median Ni and Co contents of bulk achondrites are representative of the bulk silicate portions of their parent bodies (Fig. 9).

To apply our model, we therefore relied on the hypothesis described above to estimate the bulk silicate achondrite parent bodies. Because the Ni and Co abundances of the five achondrite families are not correlated with Mg/Al, meaning that Ni and Co were not significantly fractionated during magmatic processes (Fig. 9; Palme and O'Neill, 2014), we used the median contents (excluding outliers) and median absolute deviations to define bulk silicate compositions and associate errors (Table 6, Fig. 9). We then estimated the Ni and Co contents of the APB, AuPB, NWA 7325/8486/8409 PB, NWA 011/2976 PB, and Erg Chech

Table 6
Estimated bulk silicate and bulk core compositions as well as corresponding partition coefficients for the angrite, aubrite, NWA 7325/8486/8409, NWA 011/2976, and Erg Chech 002 parent bodies.

	Bulk silicate					Bulk core					Partition coefficients			
Parent bodies	Method	Ni %	σ	Co ppm	σ	Method	Ni %	σ	Co ppm	σ	Ni	σ	Co	σ
Angrite	Med. meteor.	0.007	0.003	26.7	5.9	Mass bal. CV	5.2	2.0	2436	929	703	384	91	40
Aubrite	Med. meteor.	0.010	0.007	4.6	2.5	Mass bal. EH	7.2	2.8	3404	1311	720	560	736	490
Erg Chech 002	Med. meteor.	0.0016	0.0003	8.3	2.5	Mass bal. CI	4.2	1.6	1861	715	2633	1110	224	109
NWA 7325/8486/8409	Med. meteor.	0.0055	0.0008	17.3	2.4	Mass bal. R	7.2	2.8	3367	1292	1307	537	195	80
NWA 011/2976	Med. meteor.	0.018	0.002	41.3	1.0	Mass bal. CR	5.4	2.1	2409	913	294	116	58	22

002 PB by mass balance (Table 6). For their bulk compositions, we chose chondritic compositions considered representative of the primitive building blocks of the five achondrite parent bodies (Lodders et al., 1993; Yamaguchi et al., 2002; Jambon et al., 2011; Barrat et al., 2015, 2021; Goodrich et al., 2017; Steenstra et al., 2017; Nicklas et al., 2022; Tissot et al., 2022): CV (1.32 wt% Ni, 640 ppm Co) for the APB; EH (1.84 wt% Ni, 870 ppm Co) for the AuPB and the NWA 7325/8486/8409 PB; CR (1.38 wt% Ni, 644 ppm Co) for the NWA 011/2976 PB; and LL (1.06 wt% Ni, 480 ppm Co) for the Erg Chech 002 PB. We assumed that their cores accounted for 20–35 wt% of the PB to bracket the cases of Earth (~33 wt%), Mars (~24 wt%), and Vesta (~22 wt%; Dreibus et al., 1997), a rather unconstrained assumption resulting in large error bars. Finally, we calculated bulk core–silicate partition coefficients and associated errors (Table 6), and plotted them on the P–fO_2 model grid from Fig. 5 (Fig. 10). The P and fO_2 results for each achondrite parent body are reported in Table 7.

Our model (Fig. 10) indicates < 1 bar and IW − 1.3 for the APB, 29 GPa and IW − 5.0 for the AuPB, <1 bar and IW − 1.6 for the Erg Chech 002 PB, <1 bar and IW − 2.0 for the NWA 7325/8486/8409 PB, and 4 GPa and IW − 1.4 for the NWA 011/2976 PB (Table 7). Because the temperature during core formation is not well constrained for achondrite parent bodies, we also ran our model using two additional adiabats: one hotter and one cooler than the liquidus (described in Section 4.2, Fig. S4). In the case of achondrites, the resulting fO_2 and P values are very similar to those obtained running the model with the liquidus temperature, and identical within errors (Fig. S7). Although the modeling errors on P and fO_2 are quite large (Fig. 10, Table 7), they allow us to discuss some implications of our results.

The intrinsic fO_2 of a bulk planetary body is difficult to assess, particularly for large and geologically active planets such as Earth,

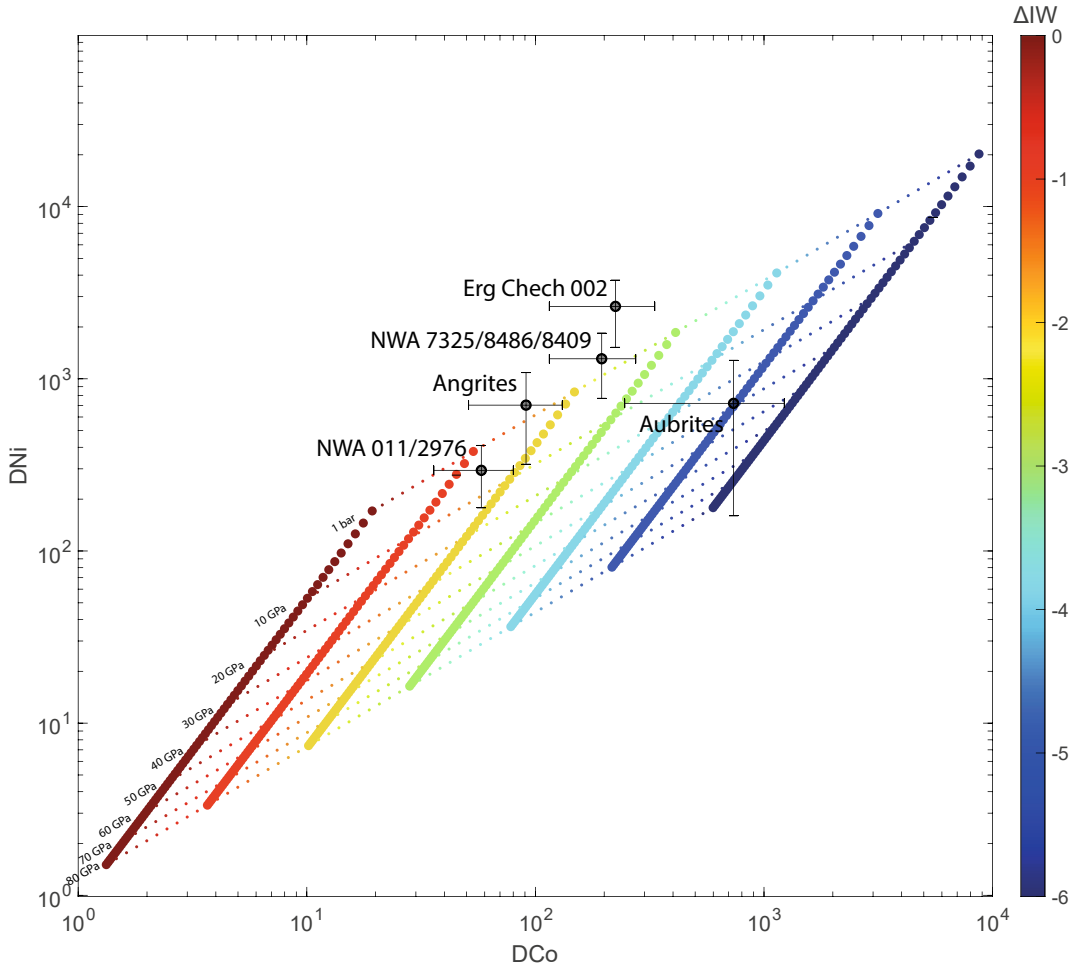

Fig. 10. Pseudo P–fO_2 space (GPa vs. ΔIW) from Fig. 5, on which are plotted the core–mantle Ni and Co $D^{met/sil}$ values calculated for the angrite parent body (APB), the aubrite PB (AuPB), the NWA 7325/8486/8409 PB, the NWA 011/2976 PB, and the Erg Chech 002 PB (Table 6) to obtain the likely thermodynamic conditions prevailing during their core formation. Results obtained are given in Table 7.

Table 7
Pressure and fO_2 results obtained by plotting achondrite parent bodies' D_{Ni} and D_{Co} in our modeled pseudo P–fO_2 space (Fig. 10). Maximum and minimum values correspond to the errors associated with D_{Ni} and D_{Co}. Parent body radii were estimated using the correlation between the Ni–Co P values and the radii of Earth, Mars, the Moon, and Vesta (Fig. 8).

Parent bodies	Estimatedradius (km)	BSFeO wt%	σ	*P*(GPa)	*P* min(GPa)	*P* max(GPa)	fO_2(ΔIW)	fO_2 min(ΔIW)	fO_2 max(ΔIW)
Angrites	≤ 263	20.2	5.9	< 0.0001	< 0.0001	9	−1.3	−2.0	−0.3
Aubrites	5420	0.05	0.03	29	14	72	−5.0	5.9	−3.0
Erg Chech 002	≤ 263	9.675	1.525	< 0.0001	< 0.0001	< 0.0001	−1.6	−2.3	−0.4
NWA 7325/8486/8409	≤ 263	0.53	0.04	< 0.0001	< 0.0001	4	−2.0	−2.7	−1.1
NWA 011/2976	2986	19.2	1.2	4	< 0.0001	13	−1.4	−1.9	−0.6

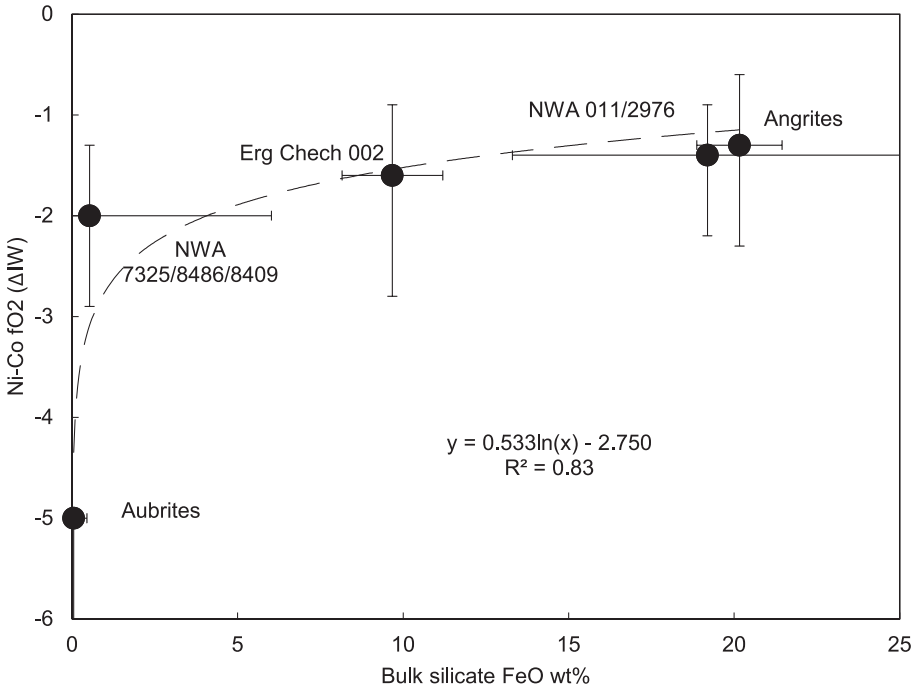

Fig. 11. fO_2 values determined from Ni–Co partitioning using our model vs. bulk silicate FeO contents of the achondrite parent bodies (Table 7).

because mineral transformations at high pressures and volatile recycling in the mantle produce rocks with a variety of fO_2. Nevertheless, the bulk silicate FeO content, established during metal–silicate differentiation, is a proxy of the bulk planet's fO_2, itself inherited from the primordial planetary building blocks and the physicochemical processes affecting them during the magma ocean stage (Righter et al., 2020). Therefore, it is not too surprising that we observe a correlation between the mean silicate FeO contents of achondrites and the Ni–Co-based fO_2 values obtained with our model, within error bars (Fig. 11). The logarithmic form of the correlation is consistent with the thermodynamic expression of $\Delta IW \propto \log_{10}(a^{sil}_{FeO})$ (Eq. (1). Moreover, our Ni–Co-based fO_2 values for the achondrite parent bodies are consistent with the fO_2 ranges of individual achondrites obtained with independent methods, such as XANES (Righter et al., 2016) and experimental petrology: ~IW − 1.5 to ~ IW + 1 for angrites (Tissot et al., 2022), ~IW − 7 to ~ IW − 5 for aubrites (Fogel, 2005; Keil, 2010), ~IW − 1.4 for Erg Chech 002 (Nicklas et al., 2022), ~IW − 3.1 to ~ IW − 2.9 for NWA 7325/8486/8409 (Goodrich et al., 2017; Sutton et al., 2017), and ~ IW − 1.4 for NWA 011/2976 (Ma et al., 2022).

We also used the empirical correlation obtained between Ni–Co-based *P* values and the radii of Earth, Mars, the Moon, and Vesta (Fig. 8) to estimate a sizes of the achondrite parent bodies based on our achondrite Ni–Co partitioning results (Table 7). Given the very large errors associated with these results (Fig. 12) and the underlying assumptions, these parent body size estimates must be taken with a grain of salt. Hence, we offer the following discussion as a starting point to investigate the properties achondrite parent bodies using our method in future, dedicated studies. From numerous attempts to estimate the APB size, conflicting arguments lead to radii from < 100 to > 340 km (Keil, 2012; Sarafian et al., 2017; Tissot et al., 2022). Our model suggests that the APB was asteroid-sized, with a radius < 263 km (Table 7); considering the errors, though, the APB could have been as large as 3,832 km in radius (Fig. 12). Similarly, our Ni–Co-based pressures for the Erg Chech 002 and NWA 7325/8486/8409 parent bodies suggest that they too were asteroid-sized, with radii < 263 km, or maximum possible radii of 263 and 2,970 km, respectively (Fig. 12, Table 7). These results are in agreement with Sturtz et al. (2022), who constrained the Erg Chech 002 parent body size to 70–130 km in radius, and with Sarafian et al. (2017) and Frossard et al. (2019), who suggested that the NWA 7325/8486/8409 parent body was a planetesimal large enough to form and retain a basaltic crust (i.e. > 100 km in radius). Our Ni–Co-based pressure estimate for the NWA 011/2976 parent body is 4 GPa, consistent with a radius of 2,986 km (Fig. 12, Table 7). Although this appears to contradict the conclusions that the NWA 011/2976 PB was a planetesimal (Yamaguchi et al., 2002; Floss et al., 2005), our error bars span radii of < 263 to 4,275 km radii. Finally, our Ni–Co-based pressures give a different case for the aubrite parent body. Indeed, the obtain pressure of 30 GPa suggests a parent body 5,420 km in radius, and the error bars span radii from 4370 to 7105 km. Therefore, based on our immediate results, either the parent body is one of the current planets, or it was destroyed after the formation of the aubrite lithologies. Many arguments support the notion that E-type asteroids, mostly located in the Hungaria

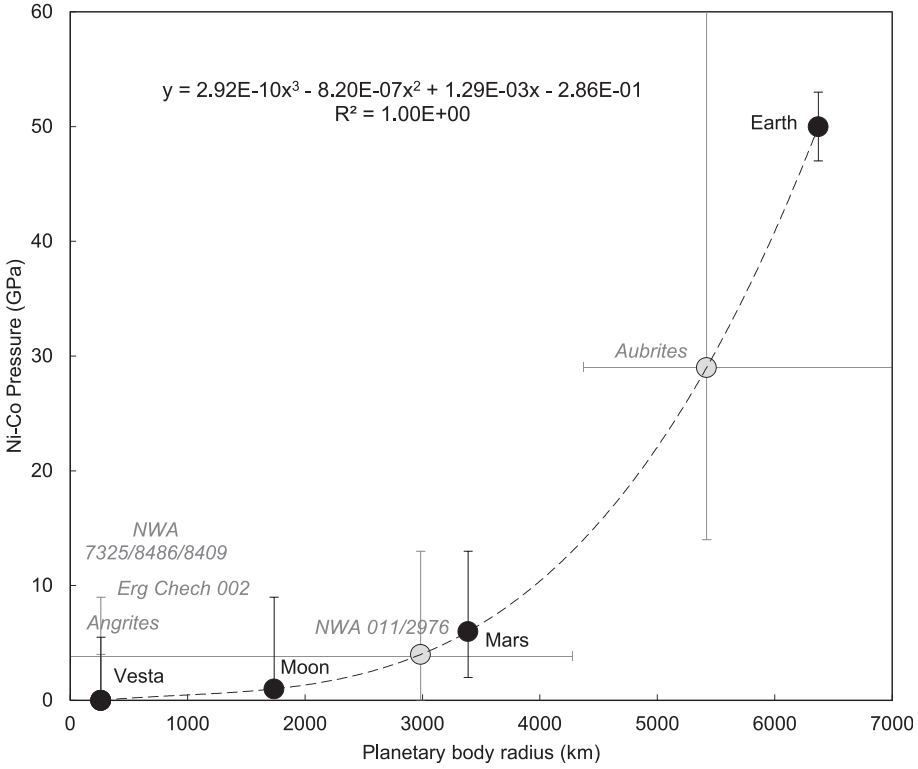

Fig. 12. Application of the polynomial regression obtained between pressures estimated from Ni–Co partitioning and planetary body radius for Earth, Mars, the Moon, and Vesta to achondrite parent bodies. The equation from Fig. 8 was solved to obtain planetary body radii for the angrite, aubrite, NWA 7325/8486/8409, NWA 011/2976, and Erg Chech 002 parent bodies based on their Ni–Co-based pressures (Table 7).

region of the main belt, are the immediate source of aubrites (Ćuk et al., 2014). We therefore propose that these asteroids could be relicts of the silicate portion of a large proto-Mercury pulverized by a giant impact. Our result that the AuPB was of intermediate size between Mars and Earth are consistent with this scenario.

5. Conclusions

This study expands our knowledge of Ni and Co as tracers of the thermodynamic conditions prevailing during core formation in planetary bodies. The metal–silicate partition coefficients of Ni and Co are strongly correlated with P and fO_2, making them reliable barometers and oxybarometers for magma ocean processes. Whereas previous calibrations were based on experiments conducted under only moderately reducing conditions similar to those on Earth and Mars, we report numerous metal–silicate partitioning experiments conducted over a range of pressures (1 bar to 26 GPa) and under highly reducing conditions (down to IW − 6.4) to expand the available Ni and Co $D^{met/sil}$ dataset. The resulting parameterization accurately predicts the evolution of $D^{met/sil}$ for Ni and Co over a broad range of conditions, encompassing pressures from 1 bar to 80 GPa, oxygen fugacities spanning IW − 6 to IW, and temperatures of 1550–4450 K. Using this parameterization, we modeled Ni and Co $D^{met/sil}$ values along the liquidus of a chondritic mantle at different P and fO_2 conditions to define a pseudo P–fO_2 space on a D_{Co} *vs*. D_{Ni} grid. We then applied this tool to investigate the thermodynamic conditions of various planetary bodies' magma oceans from their core–primitive mantle Ni and Co partition coefficients. The P and fO_2 results obtained for Earth, Mars, the Moon, and Vesta are in agreement with previous studies applying similar methods, and are strongly correlated to planetary size, supporting the reliability of our method. We then applied this tool to investigate the angrite, aubrite, NWA 7325/8486/8409, NWA 011/2976, and Erg Chech 002 parent bodies. Despite the large errors on our results, the P and fO_2 values obtained for these five achondrite families suggest a wide variety of core formation conditions, from the oxidized, asteroid-sized angrite parent body to the highly reduced, planet-sized aubrite parent body. Overall, this comprehensive study provides a model and method that can easily be applied in furthur investigations of achondrite parent body properties, or to investigate individual objects (achondrites, chondrules…) using *in-situ* Ni and Co partition coefficients.

Data availability

Tables and supplementary tables are available in a.xlsx file through "Cartier et al. Ni Co - Tables", Mendeley Data, V1, https://doi.org/10.17632/rz9htpr2rh.1 at https://data.mendeley.com/datasets/rz9htpr2rh/1. MATLAB codes to use the model are available on request from C. Cartier.

CRediT authorship contribution statement

Camille Cartier: Conceptualization, Data curation, Formal analysis, Funding acquisition, Investigation, Methodology, Project administration, Writing – original draft, Writing – review & editing. **Laurie Llado:** Investigation, Methodology, Writing – review & editing. **Hadrien Pirotte:** Investigation, Methodology, Writing – review & editing. **Laurent Tissandier:** Investigation, Methodology, Writing – review & editing. **Olivier Namur:** Writing – review & editing. **Max Collinet:** Writing – review & editing. **Shui-Jiong Wang:** Writing – review & editing. **Bernard Charlier:** Writing – review & editing.

Declaration of competing interest

The authors declare that they have no known competing financial interests or personal relationships that could have appeared to influence the work reported in this paper.

Acknowledgements

The authors thank R. Dasgupta for handling this manuscript, and D. Grewal and an anonymous reviewer for constructive comments. C. Cartier thanks R. Fischer, K. Righter, and D. van Acken for discussions, and R. Dennen for its assistance with English revisions. The IHPV and piston-cylinder experiments were supported by the von Humboldt Foundation and a Marie Curie Intra-European Fellowship (SULFURON-MERCURY – 327046). The evacuated silica tube experiments received funding from the French PNP program (INSU-CNRS). The multi-anvil experiments received funding from the European Research Council under the European Community's Seventh Framework Program (FP7/2007-2013 Grant Agreement 209035) and from the French PNP program (INSU-CNRS). The multi-anvil apparatus at the Laboratoire Magmas et Volcans is financially supported by the Centre National de la Recherche Scientifique (Instrument National de l'INSU).

Appendix A. Supplementary material

Supplementary Material includes a PDF file containing supplementary Tables S1 to S8 (except Table S7, provided as a separate .xls file) and supplementary Figures S1 to S7. This PDF includes information about the composition of starting materials used for experiments, experimental conditions, chemical composition of experimental products, tests conducted on the parametrization, adiabat calculation, tests conducted on the model using various adiabats and subsequent results. The PDF also includes supporting text for fO_2 calculation. The supplementary Table S7 is the Ni Co partition coefficients database used for the parameterization.

Supplementary material to this article can be found online at https://doi.org/10.1016/j.gca.2023.12.020.

References

Andrault, D., Bolfan-Casanova, N., Nigro, G., Lo, B.M.A., Garbarino, G., Mezouar, M., 2011. Solidus and liquidus profiles of chondritic mantle: Implication for melting of the Earth across its history. Earth Planet. Sci. Lett. 304, 251–259.

Asahara, Y., Kubo, T., Kondo, T., 2004. Phase relations of a carbonaceouus chondrite at lower mantle conditions. Phys. Earth Planet. Inter. 143, 421–432.

Barrat, J.A., Chaussidon, M., Yamaguchi, A., Beck, P., Villeneuve, J., Byrne, D.J., Broadley, M.W., Marty, B., 2021. A 4,565-My-old andesite from an extinct chondritic protoplanet. Proc. Natl. Acad. Sci. U. S. A. 118, 1–7.

Barrat, J., Greenwood, R.C., Verchovsky, A., Gillet, P., Bollinger, C., Langlade, J., Liorzou, C., Franchi, I.A., Barrat, J., Greenwood, R.C., Verchovsky, A., Gillet, P., Bollinger, C., 2015. Crustal differentiation in the early solar system : clues from the unique achondrite Northwest Africa 7325. Geochim. Cosmochim. Acta 168, 280–292.

Berndt, J., Liebske, C., Holtz, F., Freise, M., Nowak, M., Ziegenbein, D., Hurkuck, W., Koepke, J., 2002. A combined rapid-quench and H2-membrane setup for internally heated pressure vessels: Description and application for water solubility in basaltic melts. Am. Mineral. 87, 1717–1726.

Berthet, S., Malavergne, V., Righter, K., 2009. Melting of the Indarch meteorite (EH4 chondrite) at 1 GPa and variable oxygen fugacity: Implications for early planetary differentiation processes. Geochim. Cosmochim. Acta 73, 6402–6420.

Bouhifd, M.A., Andrault, D., Bolfan-Casanova, N., Hammouda, T., Devidal, J.L., 2013. Metal-silicate partitioning of Pb and U: Effects of metal composition and oxygen fugacity. Geochim. Cosmochim. Acta 114, 13–28.

Bouhifd, M.A., Boyet, M., Cartier, C., Hammouda, T., Bolfan-Casanova, N., Devidal, J.L., Andrault, D., 2015. Superchondritic Sm/Nd ratio of the Earth: Impact of Earth's core formation. Earth Planet. Sci. Lett. 413, 158–166.

Bouhifd, M.A., Jephcoat, A.P., 2003. The effect of pressure on partitioning of Ni and Co between silicate and iron-rich metal liquids: a diamond-anvil cell study. Earth Planet. Sci. Lett. 209, 245–255.

Bouhifd, M.A., Jephcoat, A.P., 2011. Convergence of Ni and Co metal-silicate partition coefficients in the deep magma-ocean and coupled silicon-oxygen solubility in iron melts at high pressures. Earth Planet. Sci. Lett. 307, 341–348.

Boujibar, A., Andrault, D., Bouhifd, M.A., Bolfan-Casanova, N., Devidal, J.-L.-L., Trcera, N., 2014. Metal-silicate partitioning of sulphur, new experimental and thermodynamic constraints on planetary accretion. Earth Planet. Sci. Lett. 391, 42–54.

Brennan, M.C., Fischer, R.A., Irving, J.C.E., 2020. Core formation and geophysical properties of Mars. Earth Planet. Sci. Lett. 530, 115923.

Briaud, A., Ganino, C., Fienga, A., Mémin, A., Rambaux, N., 2023. The lunar solid inner core and the mantle overturn. Nature 617.

Carignan, J., Hild, P., Mevelle, G., Morel, J., Yeghicheyan, D., 2001. Routine analyses of trace elements in geological samples using flow injection and low pressure on-line liquid chromatography coupled to ICP-MS: A study of geochemical reference materials BR, DR-N, UB-N, AN-G and GH. Geostand. Newsl. 25, 187–198.

Cartier, C., Hammouda, T., Boyet, M., Bouhifd, M.A., Devidal, J.L., 2014a. Redox control of the fractionation of niobium and tantalum during planetary accretion and core formation. Nat. Geosci. 7, 573–576.

Cartier, C., Hammouda, T., Doucelance, R., Boyet, M., Devidal, J.L., Moine, B., 2014b. Experimental study of trace element partitioning between enstatite and melt in enstatite chondrites at low oxygen fugacities and 5GPa. Geochim. Cosmochim. Acta 130, 167–187.

Cartier, C., Namur, O., Nittler, L.R., Weider, S.Z., Crapster-Pregont, E., Vorburger, A., Franck, E.A., Charlier, B., 2020. No FeS layer in Mercury? Evidence from Ti/Al measured by MESSENGER. Earth Planet. Sci. Lett. 534, 116108.

Cartier, C., Wood, B.J., 2019. The role of reducing conditions in building Mercury. Elements 15, 39–45.

Casanova, I., Keil, K., Newsom, H.E., 1993. Composition of metal in aubrites: Constraints on core formation. Geochim. Cosmochim. Acta 57, 675–682.

Chabot, N.L., Draper, D.S., Agee, C.B., 2005. Conditions of core formation in the Earth : Constraints from Nickel and Cobalt partitioning. Geochim. Cosmochim. Acta 69, 2141–2151.

Corgne, A., Keshav, S., Wood, B.J., McDonough, W.F., Fei, Y., 2008. Metal-silicate partitioning and constraints on core composition and oxygen fugacity during Earth accretion. Geochim. Cosmochim. Acta 72, 574–589.

Ćuk, M., Gladman, B.J., Nesvorný, D., 2014. Hungaria asteroid family as the source of aubrite meteorites. Icarus 239, 154–159.

Dehant, V., Campuzano, S.A., De Santis, A., van Westrenen, W., 2022. Structure, Materials and Processes in the Earth's Core and Mantle. Surv. Geophys. 43, 263–302.

Delano J. W. 1986. Abdundances of Cobalt, Nickel, and Volatiles in the Silicate Portion of the Moon. In: Origin of the Moon pp. 232–247.

Delbo, M., Walsh, K., Bolin, B., Avdellidou, C., Morbidelli, A., 2017. Identification of a primordial asteroid family constrains the original planetesimal population. Science. 357, 1026–1029.

DeMeo, F.E., Burt, B.J., Marsset, M., Polishook, D., Burbine, T.H., Carry, B., Binzel, R.P., Vernazza, P., Reddy, V., Tang, M., Thomas, C.A., Rivkin, A.S., Moskovitz, N.A., Slivan, S.M., Bus, S.J., 2022. Connecting asteroids and meteorites with visible and near-infrared spectroscopy. Icarus 380.

Dreibus, G., Wänke, H., 1980. The Bulk Composition of the Eucrite Parent Asteroid and its Bearing on Planetary Evolution. Zeitschrift Für Naturforsch. 35, 204–216.

Dreibus, G., Bruckner, J., Wanke, H., 1997. On the Core Mass of the Asteroid Vesta. Meteorit. Planet. Sci. A 36.

Fischer, R.A., Nakajima, Y., Campbell, A.J., Frost, D.J., Harries, D., Langenhorst, F., Miyajima, N., Pollok, K., Rubie, D.C., 2015. High pressure metal-silicate partitioning of Ni Co, V, Cr, Si, and O. Geochim. Cosmochim. Acta 167, 177–194.

Floss, C., Taylor, L.A., Promprated, P., Rumble, D., 2005. Northwest Africa 011: A "Eucritic" basalt from a non-eucrite parent body. Meteorit. Planet. Sci. 40, 343–360.

Fogel, R.A., 2005. Aubrite basalt vitrophyres: The missing basaltic component and high-sulfur silicate melts. Geochim. Cosmochim. Acta 69, 1633–1648.

Fornasier, S., Migliorini, A., Dotto, E., Barucci, M.A., 2008. Visible and near infrared spectroscopic investigation of E-type asteroids, including 2867 Steins, a target of the Rosetta mission. Icarus 196, 119–134.

Frossard, P., Boyet, M., Bouvier, A., Hammouda, T., Monteux, J., 2019. Evidence for anorthositic crust formed on an inner solar system planetesimal. Geochemical Perspect. Lett. 11, 28–32.

Gaetani, G.A., Grove, T.L., 1997. Partitioning of moderately siderophile elements among olivine, silicate melt, and sulfide melt: Constraints on core formation in the Earth and Mars. Geochim. Cosmochim. Acta 61, 1829–1846.

Gaffey, M.J., Reed, K.L., Kelley, M., 1992. Relationship of E-Type Apollo Asteroid 3103 (1982 BB) to the Enstatite Achondrite Meteorites and the Hungaria Asteroids. Icarus 100, 95–109.

Gagnon, J.E., Fryer, B.J., Samson, I.M., Williams-Jones, A.E., 2008. Quantitative analysis of silicate certified reference materials by LA-ICPMS with and without an internal standard. J. Anal. at. Spectrom. 23, 1529–1537.

Gessmann, C.K., Rubie, D.C., 1998. The Effect of Temperature on the Partitioning of Nickel, Cobalt, Manganese, Chromium, and Vanadium at 9 GPa and Constraints on Formation of the Earth's Core. Geochim. Cosmochim. Acta 62, 867–882.

Goodrich, C.A., Kita, N.T., Yin, Q.Z., Sanborn, M.E., Williams, C.D., Nakashima, D., Lane, M.D., Boyle, S., 2017. Petrogenesis and provenance of ungrouped achondrite Northwest Africa 7325 from petrology, trace elements, oxygen, chromium and titanium isotopes, and mid-IR spectroscopy. Geochim. Cosmochim. Acta 203, 381–403.

Greenwood, R.C., Franchi, I.A., Jambon, A., Buchanan, P.C., 2005. Widespread magma oceans on asteroidal bodies in the early Solar System. Nature 435, 916–918.

Hammouda, T., 2003. High-pressure melting of carbonated eclogite and experimental constraints on carbon recycling and storage in the mantle. Earth Planet. Sci. Lett. 214, 357–368.

Herzberg, C.T., Zhang, J., 1996. Melting experiments on anhydrous peridotite KLB-1: Compositions of magmas in the upper mantle and transition zone. J. Geophys. Res. Solid Earth 101, 8271–8295.

Hillgren, V.J., Drake, M.J., Rubie, D.C., 1996. High pressure and high temperature metal-silicate partitioning of siderophile elements: The importance of silicate liquid composition. Geochim. Cosmochim. Acta 60, 2257–2263.

Holzheid, A., Palme, H., Chakraborty, S., 1997. The activities of NiO, CoO and FeO in silicate melts. Chem. Geol. 139, 21–38.

Huang, D., Badro, J., 2018. Fe-Ni ideality during core formation on Earth. Am. Mineral. 103, 1707–1710.

Irving A. J., Kuehner S.M, Bunch T. E., Ziegler K., Chen G., Herd C. D. K., Conrey R. M. and Ralew S. 2013. Ungrouped mafic achondrite Northwest Africa 7325: A reduced,

iron-poor cumulate olivine gabbor from a differentiated planetary parent body. In: 44th Lunar and Planetary Science Conference pp. 2164–2165.
Isa J., Shinotsuka K., Yamaguchi A. and Ebihara M. 2008. Chemical characteristics of Northwest Africa 011 and Northwest Africa 2976. In: 71st Annual Meteoritical Society Meeting.
Jambon, A., Barrat, J., Boudouma, O., Fonteilles, M., Badia, D., Göpel, C., Bohn, M., 2011. Mineralogy and petrology of the angrite Northwest Africa 1296. Meteorit. Planet. Sci. 40, 631–375.
Jana, D., Walker, D., 1997. siderophile elements among metal and silicate liquids. Earth Planet. Sci. Lett. 150, 463–472.
Kegler, 2008. New Ni and Co metal-silicate partitioning data and their relevance for an early terrestrial magma ocean. Earth Planet. Sci. Lett. 268, 28–40.
Keil, K., 2010. Chemie der Erde Enstatite achondrite meteorites (aubrites) and the histories of their asteroidal parent bodies. Chemie Der Erde - Geochemistry 70, 295–317.
Keil, K., 2012. Angrites, a small but diverse suite of ancient, silica-undersaturated volcanic-plutonic mafic meteorites, and the history of their parent asteroid. Chemie Der Erde 72, 191–218.
Keil, K., McCoy, T.J., Wilson, L., Barrat, J.A., Rumble, D., Meier, M., Wieler, R., Huss, G. R., 2011. A composite Fe, Ni-FeS and enstatite-forsterite-diopside-glass vitrophyre clast in the Larkman Nunatak 04316 aubrite: Origin by pyroclastic volcanism. Meteorit. Planet. Sci. 46, 1719–1741.
Kilburn, M.R., Wood, B.J., 1997. Metal – silicate partitioning and the incompatibility of S and Si during core formation. Earth Planet. Sci. Lett. 152, 139–148.
Lenhart, E.M., Secco, R.A., 2022. Implications for the energy source for an early dynamo in Vesta from experiments on electrical resistivity of liquid Fe-10wt%Ni at high pressures. Icarus 378, 114962.
Li, J., Agee, C.B., 2001. The effect of pressure, temperature, oxygen fugacity and composition on partitioning of nickel and cobalt between liquid Fe-Ni-S alloy and liquid silicate : Implications for the Earth ' s core formation. Geochim. Cosmochim. Acta 65, 1821–1832.
Lodders, K., 2003. Solar system abundances and condensation temperatures of the elements. Astrophys. J. 591, 1220–1247.
Lodders, K., Fegley, B., 1998. The Planetary Scientist's Companion. Oxford Uni.
Lodders, K., Palme, H., Wlotzka, F., 1993. Trace elements in mineral separayes of the Pena Blanca Spring aubrite: Implications for the evolution of the aubrite parent body. Meteorit. Planet. Sci. 28, 538–551.
Ma, N., Neumann, W., Néri, A., Schwarz, W.H., Ludwig, T., Trieloff, M., Klahr, H., Bouvier, A., 2022. Early formation of primitive achondrites in an outer region of the protoplanetary disc. Geochemical Perspect. Lett. 23, 33–37.
Mandler, B.E., Elkins-Tanton, L.T., 2013. The origin of eucrites, diogenites, and olivine diogenites: Magma ocean crystallization and shallow magma chamber processes on Vesta. Meteorit. Planet. Sci. 48, 2333–2349.
Mann, U., Frost, D.J., Rubie, D.C., 2009. Evidence for high-pressure core-mantle differentiation from the metal – silicate partitioning of lithophile and weakly-siderophile elements. Geochim. Cosmochim. Acta 73, 7360–7386.
McCoy, T.J., 1998. A pyroxene-oldhamite clast in Bustee: igneous aubritic oldamite and a mechanism for the Ti enrichment in aubritic troilite. Antart. Meteor. Res. 11, 32–48.
McDonough, W.F., Sun, S., 1995. The composition of the Earth. Chem. Geol. 120, 223–253.
Mittlefehldt, D. W. 2014. Achondrites. In: Treatise on Geochemistry: Second Edition pp. 235–266.
Morard, G., Katsura, T., 2010. Pressure – temperature cartography of Fe – S – Si immiscible system. Geochim. Cosmochim. Acta 74, 3659–3667.
Mysen, B.O., 1983. The structure of silicate melts. Annu. Rev. Earth Planet. Sci. 11, 75–97.
Namur, O., Charlier, B., Holtz, F., Cartier, C., Mccammon, C., 2016. Sulfur solubility in reduced mafic silicate melts : Implications for the speciation and distribution of sulfur on Mercury. Earth Planet. Sci. Lett. 448, 102–114.
Nicklas, R.W., Day, J.M.D., Gardner-Vandy, K.G., Udry, A., 2022. Early silicic magmatism on a differentiated asteroid. Nat. Geosci. 15, 696–699.
Palme, H. and O'Neill, H. S. C. 2014. Cosmochemical Estimates of Mantle Composition. In: Treatise on Geochemistry: Second Edition pp. 1–39.
Paquet, M., Day, J.M.D., Udry, A., Hattingh, R., Kumler, B., Rahib, R.R., Tait, K.T., Neal, C.R., 2021. Highly siderophile elements in shergottite sulfides and the sulfur content of the martian mantle. Geochim. Cosmochim. Acta 293, 379–398.
Pirotte, H., Cartier, C., Namur, O., Pommier, A., Zhang, Y., Berndt, J., Klemme, S., Charlier, B., 2023. Internal differentiation and volatile budget of Mercury inferred from the partitioning of heat-producing elements at highly reduced conditions. Icarus 405, 115699.
Ray, S., Garvie, L.A.J., Rai, V.K., Wadhwa, M., 2021. Correlated iron isotopes and silicon contents in aubrite metals reveal structure of their asteroidal parent body. Sci. Rep. 11, 1–13.
Righter, K., 2011. Prediction of metal – silicate partition coef fi cients for siderophile elements : An update and assessment of PT conditions for metal – silicate equilibrium during accretion of the Earth. Earth Planet. Sci. Lett. 304, 158–167.
Righter, K., 2015. Modeling siderophile elements during core formation and accretion, and the role of the deep mantle and volatiles. Am. Mineral. 100, 1098–1109.
Righter, K., Chabot, N.L., 2011. Moderately and slightly siderophile element constraints on the depth and extent of melting in early Mars. Meteorit. Planet. Sci. 176, 157–176.
Righter, K., Drake, M.J., 1996. Core formation in Earth's moon, Mars, and Vesta. Icarus 124, 513–529.
Righter, K., Drake, M.J., 1997. A magma ocean on Vesta: Core formation and petrogenesis of eucrites and diogenites. Meteorit. Planet. Sci. 944, 929–944.
Righter, K., Drake, M.J., Yaxley, G., 1997. Prediction of siderophile element metal-silicate partition coefficients to 20 GPa and 2800°C : the effects of pressure, temperature, oxygen fugacity, and silicate and metallic melt compositions. Phys. Earth Planet. Inter. 100, 115–134.
Righter, K., Ghiorso, M.S., 2012. Redox systematics of a magma ocean with variable pressure-temperature gradients and composition. Proc. Natl. Acad. Sci. 109, 11955–11960.
Righter, K., Hervig, R.L., Kring, D.A., 1998. Accretion and core formation on Mars: molybdenum contents of melt inclusion glasses in three SNC meteorites. Geochim. Cosmochim. Acta 62, 2167–2177.
Righter, K., Pando, K.M., Danielson, L., Lee, C., 2010. Partitioning of Mo, P and other siderophile elements (Cu, Ga, Sn, Ni Co, Cr, Mn, V, and W) between metal and silicate melt as a function of temperature and silicate melt composition. Earth Planet. Sci. Lett. 291, 1–9.
Righter, K., Sutton, S.R., Danielson, L., Pando, K., Newville, M., 2016. Redox variations in the inner solar system with new constraints from vanadium XANES in spinels. Am. Mineral. 101, 1928–1942.
Righter, K., Herd, C.D.K., Boujibar, A., 2020. Redox Processes in Early Earth Accretion and in Terrestrial Bodies. Elements 16, 161–166.
Rivoldini, A., Hoolst, T., Van, V.O., Mocquet, A., Dehant, V., 2011. Geodesy constraints on the interior structure and composition of Mars. Icarus 213, 451–472.
Rubie, D.C., Melosh, H.J., Reid, J.E., Liebske, C., Righter, K., 2003. Mechanisms of metal-silicate equilibration in the terrestrial magma ocean. Earth Planet. Sci. Lett. 205, 239–255.
Rubie, D.C., Frost, D.J., Mann, U., Asahara, Y., Nimmo, F., Tsuno, K., Kegler, P., Holzheid, A., Palme, H., 2011. Heterogeneous accretion, composition and core – mantle differentiation of the Earth. Earth Planet. Sci. Lett. 301, 31–42.
Rubin, A.E., 1983. Impact Melt-Rock Clasts in the Hvittis Enstatite Chondrite Breccia: Implications for a Genetic Relationship Between El Chondrites and Aubrites. J. Geophys. Res. 88, 293–300.
Sarafian, A.R., Nielsen, S.G., Marschall, H.R., Gaetani, G.A., Hauri, H., Righter, K., Sarafian, E., 2017. Angrite meteorites record the onset and flux of water to the inner solar system. Geochim. Cosmochim. Acta 212, 156–166.
Siebert, J., Corgne, A., Ryerson, F.J., 2011. Systematics of metal – silicate partitioning for many siderophile elements applied to Earth ' s core formation. Geochim. Cosmochim. Acta 75, 1451–1489.
Siebert, J., Badro, J., Antonangeli, D., Ryerson, F.J., 2012. Metal – silicate partitioning of Ni and Co in a deep magma ocean. Earth Planet. Sci. Lett. 321–322, 189–197.
Siebert, J., Badro, J., Antonangeli, D., Ryerson, F.J., 2013. Terrestrial Accretion Under Oxidizing Conditions. Science 339, 1194–1197.
Stähler, S.C., Khan, A., Banerdt, W.B., Lognonné, P., Giardini, D., Ceylan, S., Drilleau, M., Duran, A.C., Garcia, R.F., Huang, Q., Kim, D., Lekic, V., Samuel, H., Schimmel, M., Schmerr, N., Sollberger, D., Stutzmann, É., Xu, Z., Antonangeli, D., Charalambous, C., Davis, P.M., Irving, J.C.E., Kawamura, T., Knapmeyer, M., Maguire, R., Marusiak, A.G., Panning, M.P., Perrin, C., Plesa, A.-C., Rivoldini, A., Schmelzbach, C., Zenhäusern, G., Beucler, É., Clinton, J., Dahmen, N., van Driel, M., Gudkova, T., Horleston, A., Pike, W.T., Plasman, M., Smrekar, S.E., 2021. Seismic detection of the martian core. Science. 373, 443–448.
Steenstra, E., 2016. Constraints on core formation in Vesta from metal-silicate partitioning of siderophile elements Constraints on core formation in Vesta from metal – silicate partitioning of siderophile elements. Geochim. Cosmochim. Acta 177, 48–61.
Steenstra, E.S., Rai, N., Knibbe, J.S., Lin, Y.H., Van, W.W., 2016. New geochemical models of core formation in the Moon from metal – silicate partitioning of 15 siderophile elements. Earth Planet. Sci. Lett. 441, 1–9.
Steenstra, E.S., Sitabi, A.B., Lin, Y.H., Rai, N., Knibbe, J.S., Berndt, J., Matveev, S., van Westrenen, W., 2017. The effect of melt composition on metal-silicate partitioning of siderophile elements and constraints on core formation in the angrite parent body. Geochim. Cosmochim. Acta 212, 62–83.
Steenstra, E.S., Seegers, A.X., Putter, R., Berndt, J., Klemme, S., Matveev, S., Bullock, E. S., Washington, D.C., 2020a. Metal-silicate partitioning systematics of siderophile elements at reducing conditions : A new experimental database. Icarus 335, 113391.
Steenstra, E.S., Trautner, V.T., Berndt, J., Klemme, S., Van, W.W., 2020b. Trace element partitioning between sulfide-, metal- and silicate melts at highly reduced conditions : Insights into the distribution of volatile elements during core formation in reduced bodies. Icarus 335, 113408.
Sturtz, C., Limare, A., Chaussidon, M., Kaminski, É., 2022. Structure of differentiated planetesimals: A chondritic fridge on top of a magma ocean. Icarus 385, 115100.
Sutton, S.R., Goodrich, C.A., Wirick, S., 2017. Titanium, Vanadium and Chromium Valences in Silicates of Ungrouped Achondrite NWA 7325 and Ureilite Y-791538. Geochim. Cosmochim. Acta 204, 313–330.
Taylor, G.J., 2013. Chemie der Erde The bulk composition of Mars. Chemie Der Erde - Geochemistry 73, 401–420.
Thibault, Y., Walters, M.J., 1995. The influence of pressure and temperature on the metal-silicate partition coefficients of nickel and cobalt in a model Cl chondrite and implications for metal segregation in a deep magma ocean. Geochim. Cosmochim. Acta 59.
Tissot, F.L.H., Collinet, M., Namur, O., Grove, T.L., 2022. The case for the angrite parent body as the archetypal first-generation planetesimal : Large, reduced and Mg-enriched. Geochim. Cosmochim. Acta 338, 278–301.
Van Acken, D., Brandon, A.D., Lapen, T.J., 2012. Highly siderophile element and osmium isotope evidence for postcore formation magmatic and impact processes on the aubrite parent body. Meteorit. Planet. Sci. 47, 1606–1623.
van Kooten, E.M.M.E., Kubik, E., Siebert, J., Heredia, B.D., Thomsen, T.B., Moynier, F., 2022. Metal compositions of carbonaceous chondrites. Geochim. Cosmochim. Acta 321, 52–77.

Wade, J., Wood, B.J., 2001. The Earth 's "missing" niobium may be in the core. Nature 409, 75–79.
Wade, J., Wood, B.J., 2005. Core formation and the oxidation state of the Earth. Earth Planet. Sci. Lett. 236, 78–95.
Wang, S.J., Li, S.J., Lin, Y., Sheng, S.Z., 2023. Mass-dependent nickel isotopic variations in achondrites and lunar rocks. Geochim. Cosmochim. Acta 350, 16–27.
Weber, I., Morlok, A., Bischoff, A., Hiesinger, H., Ward, D., Joy, K.H., Crowther, S.A., Jastrzebski, N.D., Gilmour, J.D., Clay, P.L., Wogelius, R.A., Greenwood, R.C., Franchi, I.A., Münker, C., 2015. Cosmochemical and spectroscopic properties of Northwest Africa 7325-A consortium study. Meteorit. Planet. Sci. 51, 3–30.
Wilbur, Z.E., Udry, A., McCubbin, F.M., vander Kaaden, K.E., DeFelice, C., Ziegler, K., Ross, D.K., McCoy, T.J., Gross, J., Barnes, J.J., Dygert, N., Zeigler, R.A., Turrin, B.D., McCoy, C., 2022. The effects of highly reduced magmatism revealed through aubrites. Meteorit. Planet. Sci. 34.
Wood, B.J., Wade, J., Kilburn, M.R., 2009. Core formation and the oxidation state of the Earth : Additional constraints from Nb, V and Cr partitioning. Geochim. Cosmochim. Acta 72, 1415–1426.
Yamaguchi, A., Clayton, R.N., Mayeda, T.K., Ebihara, M., Oura, Y., Miura, Y.N., Haramura, H., Misawa, K., Kojima, H., Nagao, K., 2002. A new source of basaltic meteorites inferred from Northwest Africa 011. Science 296, 334–336.
Yamaguchi A., Barrat J., Chaussidon M., Beck P., Villeneuve J., Byrne D. J., Broadley M. W. and Marty B. 2021. Petrology and geochemistry of Erg Chech 002, the oldest andesite in the solar system. In: 52nd Lunar and Planetary Science Conference.
Yen, A.S., Mittlefehldt, D.W., McLennan, S.M., Gellert, R., Bell, J.F., McSween, J.Y., Ming, D.W., McCoy, T.J., Morris, R.V., Golombek, M.P., Economou, T., Madsen, M. B., Wdowiak, T., Clark, B.C., Jolliff, B.L., Schröder, C., Brückner, J., Zipfel, J., Squyres, S.W., 2006. Nickel on Mars: Constraints on meteoritic material at the surface. J. Geophys. Res. Planets 111.
Zhu, K., Barrat, J.A., Yamaguchi, A., Rouxel, O., Germain, Y., Langlade, J., Moynier, F., 2022. Nickel and Chromium Stable Isotopic Composition of Ureilites: Implications for the Earth's Core Formation and Differentiation of the Ureilite Parent Body. Geophys. Res. Lett. 49.